SEISMIC FRAGILITY CURVE DEVELOPMENT OF AN ONSHORE WIND TURBINE INCORPORATING SOIL STRUCTURE INTERACTION EFFECTS

by

Özgün Ergün

B.S., Civil Engineering, Boğaziçi University, 2016

Submitted to the Institute for Graduate Studies in
Science and Engineering in partial fulfillment of
the requirements for the degree of
Master of Science

Graduate Program in Civil Engineering

Boğaziçi University

2018

ACKNOWLEDGEMENTS

I would like to express my sincere gratitude to Associate Professor Serdar Soyöz for his supervision, encouragement and support during development of this work. It was an honor and a rewarding learning process for me to work with him.

I would also like to thank Associate Professor Kutay Orakçal and Assistant Professor Barlas Özden Çağlayan for accepting to become my committee members. Their valuable comments were enlightening.

My colleagues Emre Aytulun, Oğuz Şenkardeşler and Semih Gönen deserve a special thanks for sharing their experience and knowledge with me. I would also like to thank my fellow researcher Serap Hanbay for our productive discussions and her voluntary involvement in site visits.

I was lucky that my friends for many years and outstanding engineers Barış Elmas, Cihad Alp Göroğlu, Sefa Handere and Fehmi Alp Vurnal were by my side.

The support of my dear parents and sister were endless. Their faith in me has always been the driving force in my educational and academic life.

I am indebted to my girlfriend Jennifer for her support, love and patience during the stressful times on this path.

ABSTRACT

SEISMIC FRAGILITY CURVE DEVELOPMENT OF AN ONSHORE WIND TURBINE INCORPORATING SOIL STRUCTURE INTERACTION EFFECTS

In this study, a 900 kW onshore wind turbine supporting structure was modelled with finite elements in ANSYS software to perform nonlinear time history analyses. The structure has a tubular steel tower of 54 meters high, foundation with 26 reinforced concrete piles. The mass from rotor, nacelle and hub were applied to tower top as point mass with eccentricity. To incorporate soil-structure interaction effects, three different modelling approaches were used. Firstly, the soil medium was modelled explicitly together with piles and superstructure. The uncertainty related with the elasticity modulus of the soil was discussed by comparing the mode frequencies from finite element model with varying soil elasticity modulus values to those obtained by FDD of ambient vibration response from the accelerometers on the tower. In the second model, the load-deformation relationships obtained by static nonlinear pushover analysis were defined in soil springs under the tower. Lastly, py, tz and qz springs attached to the piles were used to model soil properties. Three ground motion records were selected in accordance with 2018 Turkish Earthquake Resistant Building Design Guideline. Nonlinear time histories were applied to the three models and their responses were compared. Then, choosing one of the modelling approaches, fragility curves for the structure were constructed with limit states being tower drift and steel local buckling. The results showed tower drift to be the governing limit state. The failure probabilities for local buckling for the same PGA values were found to be much lower than for tower drift.

ÖZET

KARA TİPİ BİR RÜZGAR TÜRBİNİ İÇİN YAPI ZEMİN ETKİLEŞİMİNİ KAPSAYAN DEPREMSEL KIRILGANLIK EĞRİLERİNİN OLUŞTURULMASI

Bu çalışmada, 900 kW kara tipi bir rüzgar türbininin taşıyıcı sistemi sonlu elemanlarla ANSYS yazılımında modellenmiştir ve doğrusal olmayan zaman tanım alanında hesap yapılmıştır. Modellenen yapı 54 metre yüksekliğinde boru tipi çelik kesite ve 26 adet betonarme kazığa sahiptir. Türbinin kule harici mekanik kısımlarının kütlesi, dışmerkezlik hesaba katılarak noktasal kütle olarak modelde tanımlanmıştır. Yapı-zemin etkileşimi etkilerini de hesaba dahil etmek amacıyla 3 farklı modelleme yaklaşımı kullanılmıştır. İlk modelde, zemin ortamı 3 boyutlu olarak kazıklarla ve üstyapıyla beraber modellenmiştir. Zemin elastisite modulü ile alakalı belirsizliği gidermek için, farklı elastisite modulü değerleri kullanılarak elde edilen mod frekansları ile yapıda yerleşik bulunan ivmeölçerlerden elde edilen ivme kayıtlarının FDD analizi yapılarak bulunan mod frekansları karşılaştırılmıştır. İkinci modele, statik itme analiziyle elde edilen yük-şekil değiştirme ilişkileri zemin yayları aracılığıyla kule altına yerleştirilmiştir. Son modelde, py, tz, qz yayları kazıklar boyunca 6 serbestlik derecesinde etkili olacak şekilde tanımlanmıştır. 2018 Türkiye Bina Deprem Yönetmeliğine göre seçilmiş 3 bileşenli yer hareketi kayıtları farklı modellere uygulanmış ve sonçlar karşılaştırılmıştır. Sonrasında, bir model seçilerek türbin kule yapısı için kırılganlık eğrileri oluşturulmuştur. Kırılganlık eğrisi oluşturmak için seçilen limit durumlar kule ötelenmesi ve yerel burkulmadır. Sonuçlar kule ötelenmesinin daha kritik olduğunu göstermiştir. Aynı maksimum yer ivmesi değerlerine karşılık gelen çökme olasılıkları yerel burkulma için kule ötelenmesinden daha düşük bulunmuştur.

TABLE OF CONTENTS

LIST OF FIGURES

LIST OF TABLES

LIST OF SYMBOLS

A	Factor to account for static or cyclic analysis
c	Undrained shear strength for undisturbed clay soil samples
C	Critical elastic buckling coefficient
D	Section outer diameter
E	Modulus of elasticity
f_1	Fundamental frequency of vibration
F_1	Seismic site coefficient for 1 second period region
F_S	Seismic site coefficient for short period region
F_{xc}	Inelastic local buckling stress
F_{xe}	Elastic local buckling stress
F_y	Yield stress
J	Dimensionless empirical constant
g	Gravitational acceleration
GPa	Gigapascal
GW	Gigawatts
H	Depth below ground
Hz	Hertz
k	Initial bearing capacity
kW	Kilowatts
kg	Kilogram
km	Kilometers
kN	Kilonewton
kPa	Kilopascal
ln	Normal logarithm
m	Number of intensity measure levels
mm	Milimeters
MPa	Megapascal
M_w	Moment magnitude

MW	Megawatts
N_q	Dimensionless bearing capacity factor
n_j	Number of ground motions with $PGA = x_j$
p_o	Effective overburden pressure
p_u	Ultimate bearing capacity
p_{ud}	Deep ultimate bearing capacity
p_{us}	Shallow ultimate bearing capacity
q	Unit end bearing
Q	Mobilized end bearing capacity
Q_p	Total end bearing
S_1	1 second period horizontal spectral acceleration from PGA map
S_{ae}	Horizontal elastic spectral acceleration
S_{aeD}	Vertical elastic spectral acceleration
S_{D1}	1 second period design spectral acceleration
S_{DS}	Short period design horizontal spectral acceleration
S_S	Short period horizontal spectral acceleration from the PGA map
t	Mobilized soil pile adhesion
t_{max}	Maximum soil pile adhesion
T	Natural period of vibration of the structure
T_1	Fundamental period of vibration
T_A	Horizontal design spectrum corner period
T_{AD}	Vertical design spectrum corner period
T_B	Horizontal design spectrum corner period
T_{BD}	Vertical design spectrum corner period
T_L	Horizontal design spectrum transition period to constant displacement zone
T_{LD}	Vertical design spectrum transition period to constant displacement zone
y	Lateral deflection
X	Depth below soil surface

X_R	Depth below soil surface to bottom of reduced resistance zone
x_j	Discrete intensity measure values
z	Local pile deflection
z_j	Number of collapses under ground motions with $PGA = x_j$
α	Maximum skin friction coefficient
β	Standard deviation
ε_c	Strain which occurs at one-half the maximum stress on laboratory undrained compression tests of undisturbed soil samples
θ	Median
Φ	Standard normal cumulative distribution function
Π	Product sign
γ	Effective soil unit weight

LIST OF ACRONYMS/ABBREVIATIONS

3D	Three Dimensional
AFAD	Disaster and Emergency Management Authority
API	American Petroleum Institute
BNWF	Beam on Nonlinear Winkler Foundation
CDF	Cumulative Distribution Function
FC	Fragility Curve
FDD	Frequency Domain Decomposition
GWEC	Global Wind Energy Council
IM	Intensity Measure
PEER	Pacific Earthquake Engineering Research Center
PGA	Peak Ground Acceleration
PGD	Peak Ground Displacement
RSN	Record Sequence Number
SRSS	Square Root of Sum of Squares
SSI	Soil-Structure Interaction
TBDY	Turkish Earthquake Resistant Building Design Guideline
TUREB	Turkish Wind Energy Association

1. INTRODUCTION

1.1. Objective

The aim of the work presented in following pages is to perform vulnerability estimation by developing seismic fragility curves for an onshore wind turbine located in Boğaziçi University Sarıtepe Campus. For developing the fragility curve, soil structure interaction effects are also considered. The analyzed wind turbine has a rated power of 900 kW, hub height of 54 meters, steel tubular cross section tower, and a foundation with a pile group consisting of 26 reinforced concrete piles. The site is located in Northern Istanbul, 41 km's away from the North Anatolian Fault's Marmara segment. The structure is located on a site with silty clay and sand. In addition to purpose of developing fragility curve, another aim in this study is to compare and assess three different modelling approaches for SSI effects on structures with pile foundations. Three approaches are referred in this thesis as Continuum Model, Global Springs Model and API springs Model. The modelling approaches are compared in terms of similarity of their results, the ease of modelling and computational time they require.

The decision to develop fragility curves for vulnerability assessment was made because they provide a probabilistic cause effect relationship that would be needed by any investor prior to the decision of selection of a site for wind power plant construction. Also, as described further in Chapter 2., the regions of Turkey with high wind energy harnessing potential are also regions with high seismicity. There are several agreements among Turkish Ministry of Energy and wind power plant manufacturers that have been made recently on installing numerous wind power plants in Turkey and the seismicity of the country must be included on the planning stage of the wind farms to be constructed.

The loading examined in this work is only due to earthquake. Operational loads from the wind drag are not included in the demands. The event of an earthquake was theoretically considered as the blades of the wind turbine being positioned into idling mode. Meaningly, each blade rotating around their longitudinal axes in a specific angle

of attack position to minimize drag and lift forces. The wind turbine model considered in this work is capable of automatically activating the idling mode, or in other words blades pitching themselves into the idling mode -as defined in product specifications- within seconds. Considering the early warning system with 10 stations located around the Marmara Sea, Erdik [1] suggested early warning prior to the event by as much as 8 seconds could be possible for Istanbul depending on the location of the rupture [2]. A theoretical condition of early warning and wind rotor emergency stop was considered in this thesis.

1.2. Literature Review

There is plenty of work in the literature related to earthquake resistance of wind turbines. The spectrum of the broad range of literature involves onshore and offshore wind turbines, wind turbines with monopile foundations, with foundations having several piles and as well as with shallow foundations. The subject of this thesis is a wind turbine having a foundation with several piles. Therefore, the literature related to non-linear soil structure interaction in time domain and several modelling approaches were read and summarized for this chapter. In addition to the soil structure interaction, literature on failure of wind turbines and on reliability analysis using fragility curves are also examined.

Kausel [3] summarized the early history of soil-structure interaction. According to his summary, the principal problems encompassed by the SSI theory include:

(i) Response of a soil domain to external static or dynamic sources acting on or near the surface. The sources can be concentrated, distributed, harmonic in time or suddenly applied.

(ii) Response of the soil to ground-borne vibrations caused by earthquakes or other sources such as trains.

(iii) Response of rigid, theoretically massless structures to ground waves passing underneath. This is called kinematic interaction as well.

(iv) Response of theoretically massless footings embedded in surrounding soil excited by static, harmonic or transient loads applied directly on them.

(v) Additional deformation of surrounding soil due to the response of the structures own inertia. This is also called inertial interaction.

To solve the above problems first half on 20th century, researchers tried to derive analytical solutions for the idealized problems such as circular disks welded on elastic half spaces. With the introduction of digital computers and numerical methods such as finite elements in the 1960s and 1970s, it was possible then to focus on numerical solutions for deformations of foundations of arbitrary shapes rather than purely analytical methods. It was even possible to account for the inelasticity of the soil.

Otoniel Diaz and Luis E. Suarez [4] prepared an analytical model of an operating wind turbine to obtain the earthquake response due to three base accelerations combined with operational conditions. Their model considers the flexibility of the blades and the tower. They chose a turbine with hub height of 77 meters and a rated power of 1.65 MW. They considered the aerodynamic damping from the blades and 1% of critical damping for all modes of the tower. Their results showed that the turbine was susceptible to more damage along side to side direction due to lack of aerodynamic damping from the blades in this direction. Critical stresses occurred on the tower when extreme wind was combined with chosen earthquake motions. They did not observe flapping of the blades that could cause a crash of blades with the tower. Also, they did not observe critical stresses on the blades.

Atul Patil *et al.* [5] used finite element to model a wind turbine with a rated power of 1.65 MW and 80 m hub height. They did not explicitly model rotor blades and nacelle but used an equivalent point mass instead. They considered the detailing in tower modelling such as flanges and door openings in case the failure can happen around these places. The writers define their models being as both conservative and nonconservative. Conservative in terms of they ignore the aerodynamic damping from the blades and nonconservative due to ignoring the forces from wind to the rotating blades and to the tower. They included nonlinearity as material nonlinearity of the

tower and geometric nonlinearity from large deflections. For the fragility analysis, the limit states chosen were global buckling, overturning of the foundation, the first yielding and permanent deformation after the earthquake. They used two sets of earthquake records for nonlinear time history analyses one set being near-fault and the other set being far-fault. The results showed that the tower was most vulnerable to overturning, then yielding of the tower, permanent deformation, and global buckling respectively from most to least vulnerable.

Baniotopoulos *et al.* [6] presented details on analysis and design of a 1 MW prototype wind turbine. two different modelling approaches were compared for the analysis of seismic, wind and gravity loading of the structure. Also, fatigue analysis was performed and Eurocodes were followed for the analyses. They found it significant that for mode shapes and frequencies, a simple linear analysis was sufficient where local stress analyses should be handled with care. Seismic loads were only of importance on seismicly hazardous sites with soft soils underground.

Bazeos *et al.* [7] analyzed a 450 kW wind turbine tower under gravitational static, seismic and aerodynamic loading. The puspose was to assess the design being succesful in accordance with recommendations from several building codes. Buckling was considered as the limit state and placing soil springs under the structure and their effect on overall analysis was discussed. The simplified design approaches from building codes were found sufficient to model operational and seismic loading but it was also found that the boundary conditions between sections of the tower should be handled carefully.

Mensah *et al.* [8] gave suggestions on how to combine operational and seismic loading subjected on a 5 MW wind turbine. The method was to combine stochastic wind loads with historical earthquake records and simulating structural responses. The simulation aimed to assess load combination requirements for operational and earthquake codes. The effects of seismic loads were found to be significant considering the bending moments they create on the tower at about 2/3 of the tower height from ground. The wind loading was not found to be significant considering active pitch

control on the modern wind turbines since the pitch control revolves the blades in a position to not take any drag or lift forces when the wind speed exceeds some limit predefined in the turbine's memory.

Nuta *et al.* [9] discussed a methodology for seismic risk assessment of steel tubular tower wind turbines. A 1.65 MW wind turbine was modelled implicitly with finite elements and incremental dynamic analysis was performed. The damage limit states were defined as 0.2% residual tilt, 1.0% residual tilt, first buckling and first yield of the tower. Then, after conducting incremental dynamic analysis the fragility curves were developed for each damage state. The location of the wind turbines were chose thus the ground motion records were chosen to vary between high and low seismicly active regions. Though the differences were significant among these regions, the earthquake load was found as not resulting with dangerously high tower demands.

Witcher *et al.* [10] combined aerodynamic and seismic loading by subjecting them on the tower in the time domain. They outlined a procedure and presented a code for performing the outlined procedure. The procedure was preparing a design spectrum for the structure and then producing synthetic time history records suiting to the prepared spectrum and then applying them on the structure to calculate responses. Then, the results were compared to that obtained from frequency domain analysis and results were found not to deviate significantly.

Zaaijer *et al.* [11] discussed foundation modelling approach for offshore wind turbines. Three different foundation types for offshore wind turbines were considered. These are tubular tower on a monopile, tripod and tubular tower with piles and lattice tower with piles. The supports were designed for a 3 MW wind turbine. A reference model was constructed with py, tz and qz springs. Then the other modelling approaches were compared with the reference model in terms of the modal properties they give. Three modelling methods were effective fixity length, stiffness matrix for foundation and uncoupled springs.

Katsanos *et al.* [12] focused on the trends in the professional and academic fields in terms of the structural analyses of the wind turbine towers and which exposure types are considered during design. They stated the general approach being the main exposure considered was solely wind. This was mostly due to the stock until the last years worldwide not being on the earthquake prone areas of the world. However, with recent installations in China, India, South Korea, Southern Europe and Middle East as of 2016, the earthquake resistance should be a primary topic of analyses for the wind turbines. The writers pointed out the general opinion that the tall slender structures that have a high natural period of vibration compared to other structures are somehow "self-isolated" therefore they did not undergo severe load demands under earthquakes. In addition, there were not many cases of wind turbine failure due to earthquakes. It is disagreed in the paper by focusing on the low numbers that had been installed in seismically active zones and the low numbers of exposures to the severe events. The concentration of wind power plants in earthquake producing regions is relatively new and overlooking can be too deceiving. Motivated from the fear of overlooking such outcomes, the writes tried to investigate the potential weak spots that wind towers can have against earthquakes by reviewing the literature written mostly after 2000. Their review pointed out that unlike the popular opinion of wind turbines being slender and therefore "earthquake repellent", in many cases the earthquake load is driving the designs in seismic zones. Some severe damage types were overturning moments, high steel stresses that can exceed yield strength, soil compliance and therefore resonance risk.

Prowell *et al.* [13] conducted shake table tests on 23 m high wind turbines with 65 kW power capacity. The motivation for their study was the scarcity of the experimental validation of theories in the field. During all the shakings, the rotor was parked therefore they did not include operational effects. They investigated damping with logarithmic decrement method and found it to be less than 1% critical for the first mode. In addition, they used the response data from installed accelerometers on the turbine and produced transfer functions to obtain mode shapes. They prepared two finite element beam-column models one with rotor, nacelle being assigned as point masses and the other where these parts being modelled explicitly. The two models

gave reasonably close mode frequencies and shapes for the first and second bending mode. The third bending mode however was different for both cases and could not be compared with the experimental mode since it was not possible to obtain.

Taddei *et al.* [14] proposed a practical soil-structure interaction model simulating an emergency shutdown in case of earthquake. They reminded that the best practice combination of operational demands and earthquake demands is such that the higher of normal operational demands and characteristic demands during an emergency stop should be superposed with seismic demands. They modelled the tower as an Euler-Bernoulli beam with lumped mass and assumed the tower would stay in elastic range thus superposition principle would be applicable. Soil effects were considered for earthquake motions with foundation springs where for operational demands the tower was considered as fixed based.

Austin *et al.* [15] investigated the soil-foundation-structure interaction on the seismic response of wind turbines. They modelled three wind turbines with rated powers of 65 kW, 1 MW, and 5 MW. They followed varying approaches in terms of foundation design and modelling. They modelled the foundation implicitly with subgrade modulus springs and explicitly with surrounding soil. Also, several foundation designs were compared. These were spread foundation, monopile, pile group with cap, and anchored spread foundation. They found out as results of this study, minor increases in demand were observed when soil-structure interaction was considered compared to fixed base case. Also, the writers stated that the implicit modulus of subgrade reaction model was accurate enough just as the explicit soil model in terms of the response from the structure and it was more advantageous being easier to model and quicker to solve.

Prowell *et al.* [16] modelled a 5 MW wind turbine to observe the influence of soil structure interaction. They modelled a fixed based beam-column model first, then a detailed 3D structure with soil. 3D model's turbine parts, meaning the tower and blades were modelled as beam-column elements as well. The soil on the other hand was modelled by elastic solid elements. They observed the effect of soil on the tower overturning moment and base shear with changing soil stiffness and soil thickness from

3 to 15 meters. The model was subjected to 1994 Northridge earthquake event. Their conclusion showed that SSI effects did not turn out to be significant for stiff soils. For soft soils however, the turbine shear and moment demand increased. The modal parameters also changed on soft soils even though the differences were not major.

Kennedy *et al.* [17] was the first to use fragility functions in earthquake engineering. They defined the fragility function as the probabilistic relationship between the possibility of occurrence of failure of a nuclear power plant and the peak ground acceleration of an earthquake that it is being subjected. To put it more directly, fragility function can be defined as the possibility of some unwanted outcome to occur with respect to the governing damage causing effect of an environmental event.

Porter [18] provided a guideline for engineers that are interested in a primer for earthquake related fragility, vulnerability, and risk. The target of his work was those studying natural hazard risk and catastrophe risk modelling. He defined the parameters required to quantify risk in the eyes of an engineer. He also provided detailed definitions and explanations with examples for many probabilistic and statistic terms and their use in engineering.

Mylonakis and Gazetas [19] investigated the soil structure interaction in that whether it was beneficial or detrimental to the structure. The common perspective in this subject prior to their publication was that the elongated natural period of a structure with respect to infinitely rigid based structures due to soil flexibility had a beneficial effect by reducing the demands. It was logical since almost all earthquake spectra had a descending response branch with higher structural periods. However, this publication showed that increased period does not necessarily decrease demands. The response can be varying for different earthquake records. Therefore, the conventional approach was an oversimplification. On soft soils, the increased natural period showed increased demands with SSI.

Shaomin Wang *et al.* [20] investigated analytical design tools for modelling soil structure interaction. They used several derivatives of “Beam on Nonlinear Winkler

Foundation" (BNWF) method to predict results of centrifuge tests of single piles in soft clay soil profile. They compared several arrangements of p-y springs and dashpots to model stiffness and radiation damping properties. Their conclusion showed that the most favorable arrangement would be placing linear viscous dashpots in series with the linear component of p-y element.

M. Asareh [21] investigated the dynamic behavior of a 5 MW wind turbine under aerodynamic and seismic loading by constructing a fragility curve with damage states defined as top displacement exceeding 1.25% tower height, 5° rotation at rotor, 1% tower height residual deformation, exceeding yield stress and global buckling. Among them, tower top displacement was found out to be governing damage state.

Mo *et al.* [22] used fragility analysis to assess the vulnerability of an off-shore 5 MW wind turbine with monopile foundation. They modelled soil structure interaction effects using the beam on nonlinear Winkler foundation (BNWF) method. Nonlinear time history analyses were used to determine the probabilities of exceedance of certain damage states with varying engineering demand parameter being PGA. Controlled damage states were 1.25% tower height top displacement, 2.5° rotation of rotor, allowable stress of connecting piece steel material and tower yield stress. The fragility analyses indicated that governing damage states were nacelle displacement and rotation.

1.3. Scope

The second chapter gives information about the wind power use around the world and in Turkey. The installment of new wind turbines in recent years in earthquake prone areas is discussed.

The third chapter is focused on the modelling approaches used for this thesis. The details of the models are given. The three modelling approaches used in this work are referred to as:

- Continuum Model
- Global Spring Model
- API Spring Model

The assumptions and material modelling for the three types are detailed in this chapter as well as comparisons of structural frequencies with each other and with those obtained from actual response of the structure. Details are given on modelling in ANSYS software.

In the fourth chapter, Nonlinear Dynamic Time History Analysis is discussed. Details on developing design spectra and choice of ground motion records accordingly are given. Details and purpose of developing fragility curves are also given in this chapter. The failure modes considered on the development of fragility curves are detailed.

The fifth chapter gives the conclusion and comments on the obtained results, possible improvements on the modelling techniques, and discusses what else can be added for future work.

2. WIND ENERGY

2.1. History of Wind Energy

The history of wind power involves an extensive transformation from early simple devices to modern sophisticated machinery. The working principle of wind energy harnessing devices can be defined by drag and lift forces. A streaming fluid exerts force to any object that it surrounds and that has a relative speed with respect to the fluid. Drag is the component of this force that is along the stream and lift is the component perpendicular to the stream. It can be understood easily on an aircraft foil. The accelerating aircraft has a relative speed with respect to the air surrounding it. Thanks to the aerodynamic properties of the airfoils, the lift forces overcome gravity. The same is true for a wind turbine blade. The flowing wind exerts drag force on the blade that is opposed by the tower of the turbine fixed to the earth and the lift force that is not opposed which results with the rotor rotation. The free body diagram of an airfoil is shown on Figure 2.1.

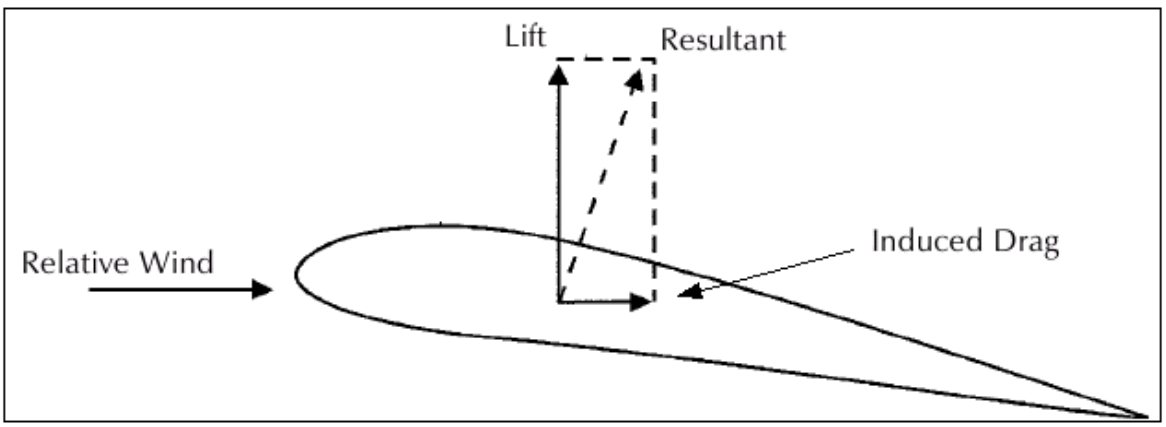

Figure 2.1. Free Body Diagram of an Airfoil [23].

By 11th century, wind power was being used in the Middle East for grain grinding and water pumping. The vertical shaft of the rotor was fixed to a grinding stone enclosed by a building. Crusaders and merchants took the idea of using the wind power to Europe. The early European windmills had a horizontal axis unlike their

predecessors. This was a huge step in design that made it more efficient with faster rotation. The reason of horizontal axis wind turbines being superior to the earlier Persian ones is that they take advantage of all swept area where Persian windmills had shielding on half of the blades [24].

Figure 2.2. An Early European Horizontal Axis Windmill [24].

The windmills were developed over centuries to be more efficient and strong. But their purposes of use remained as mechanical tasks such as water pumping, irrigation, grinding grains, saw milling of timber and powering tools. All the designs had wooden blades with changing numbers and sizes. The steel blades were first used in United States in 1870. Steel blades had the huge advantage of being lighter and shapeable into efficient forms. They worked so well that their high speed needed a reduction gear to drop to operating speeds [25].

The first example of using wind power to generate electricity dates to the end of 19^{th} century in the United States. In the late 19^{th} and early 20^{th} century, there was progress in Europe as well in generating electricity from wind power. In Germany, Professor Ulrich Hutter developed several medium size horizontal axis wind turbines

Figure 2.3. A Steel Blade Water Pumping Windmill [25].

that had modern airfoil-type fiberglass. He was the first to use fiberglass composite blades. They provided lighter weight compared to steel blades.

Professor Hutter came up with the idea of "wind farms" and realized this in 1950's. He was one of the people laying foundation stone for the development of modern wind turbines and wind farms [26].

In the 1960's, the low prices of fossil-fuel threw wind energy out of focus. Wind turbines weren't competitive with steamed-powered generating plants. In 1978 however, the US federal government passed an act requiring electric utilities to interconnect with small power generators employing renewable energy sources and to purchase their generated power at "avoided cost". Also, the policy exempted renewable energy generators from certain utility regulations. Within next years, thousands of wind turbines were installed in California. The developed technology on materials science, computer science, aerodynamics and analysis methods have made it possible to increase year by year the efficiency and capacity of newly designed wind turbines. Wind energy is now one of the fast-growing sectors in renewable energy that encircles multidisciplinary work of several engineering and science branches.

Figure 2.4. Ulrich Hutter's Wind Turbine Was Advanced for its Time.

2.2. Wind Energy Around the World

Wind energy sector is a fast growing renewable energy sector that is proved to be environmentally friendly, reliable and affordable. Historically, the use of wind energy was adopted to grind grains, pump water, sailing the seas. With the other developments in technology it is not common anymore to use windmills for water production works but it can be stated that the most effort about the wind goes to harnessing electricity out of it.

Although the first example of using wind to produce electricity dates back to 19^{th} century, the reliable and efficient electricity production matured in 1980's. Now it is used all around the world with on-shore and off-shore wind farms working continuously.

The globally installed wind power in total is 539 Gigawatts as of the end of 2017 [27]. The growth in the market in 21^{st} century is nonstop. In 2015, there was a record high new installations of wind turbines with the total power of 64 Gigawatts. Figure

2.5 [27] shows the annual addition of capacity global, and the cumulative capacity over years.

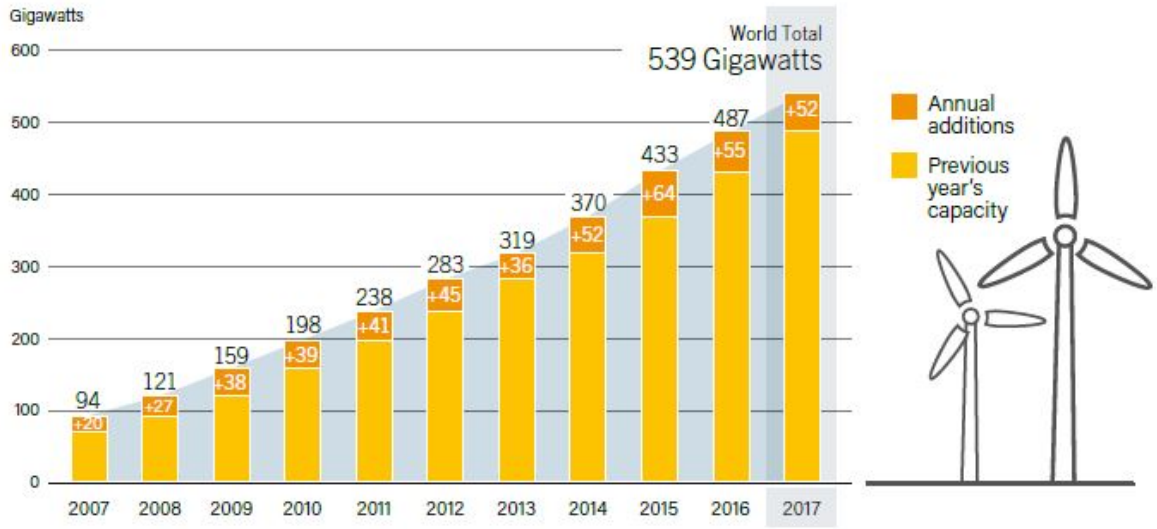

Figure 2.5. Wind Power Global Capacity and Annual Additions, 2007-2017.

The growth of the capacity is due to renewable energy related policies, cost-competitiveness, and its potential environmental and other benefits. The decreasing prices for wind power made it a low-cost option for power generation in a large number of markets [28].

Asia has been the largest regional market for wind power for the last 9 consecutive years as of 2017, representing about 48% of all added capacity. Europe follows by 30%. China is the leading country with total capacity and the new installations by 2017 as shown in Figure 2.6 with top 10 countries listed by total capacity. Although not shown in the figure because of lower total capacity, Turkey was in top 10 in 2017 in terms of the new installed power [29].

Wind power is contributing a significant share of electricity production in an increasing number of countries. In 2017, wind energy covered about 11.6% of EU yearly electricity consumption. More than 10 countries around the world cover at least 10% of their annual electricity consumption by wind power. Globally, wind power

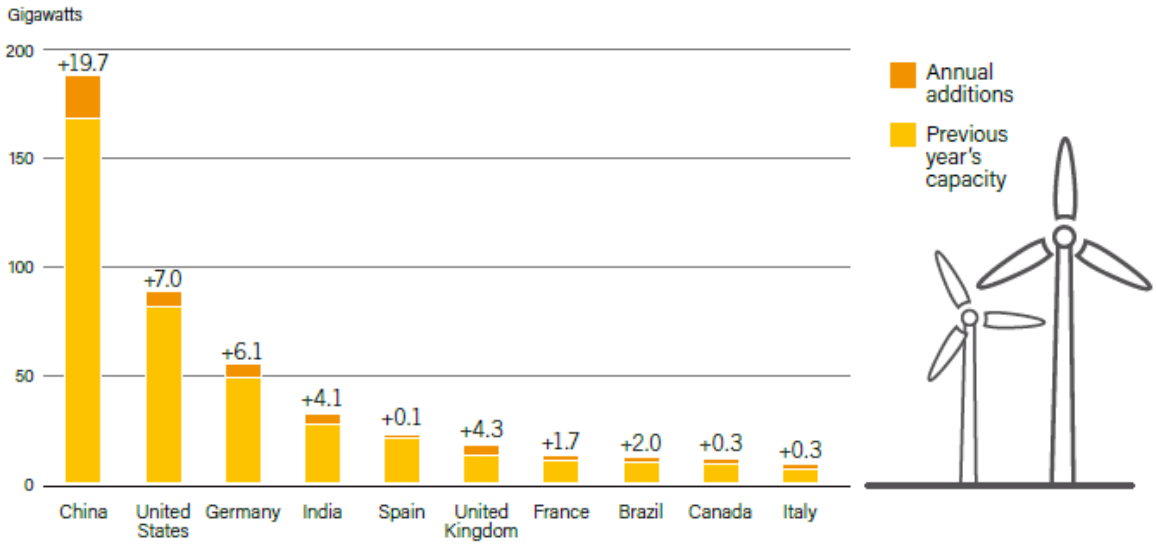

Figure 2.6. Wind Power Capacity and Additions, Top 10 Countries, 2017.

capacity operation is to account for an estimated 5.6% of total electricity generation.

The general trend of increasing the newly developed and designed wind turbine capacity was same as before in 2017. Meaning longer blades, larger rotor size, higher hub heights as a results of the aim for boosting the output and gain to maintain or increase their market share. The capacity of off-shore wind turbines is larger than their on-shore versions due to the land regulations for on-shore turbines. The increased capacity per turbine is advantageous for the manufacturers since larger turbines mean fewer foundations, converters, cables and other resources need for the same output; this translates into higher profitability. In Europe, the average turbine sizes including on-shore and off-shore installed in 2017 was 3.1 MW, whereas the off-shore average was 5.9 MW.

The market projections for 2018-2022 interval (Figure 2.7) by Global Wind Energy Council forecast 840 GW of total installed wind power by 2022. It was about 40 GW per year newly installed wind power globally between 2009-2013. 50 GW barrier was broken through in 2014. The industry set the record of more than 60 GW in a year in 2015 due to extraordinarily high numbers of installments in China. In 2016

the market declined to 54 GW and in 2017, the numbers were close to the year before. GWEC expects similar numbers for 2018 but they also estimate a growth afterwards due to 2020 targets [30].

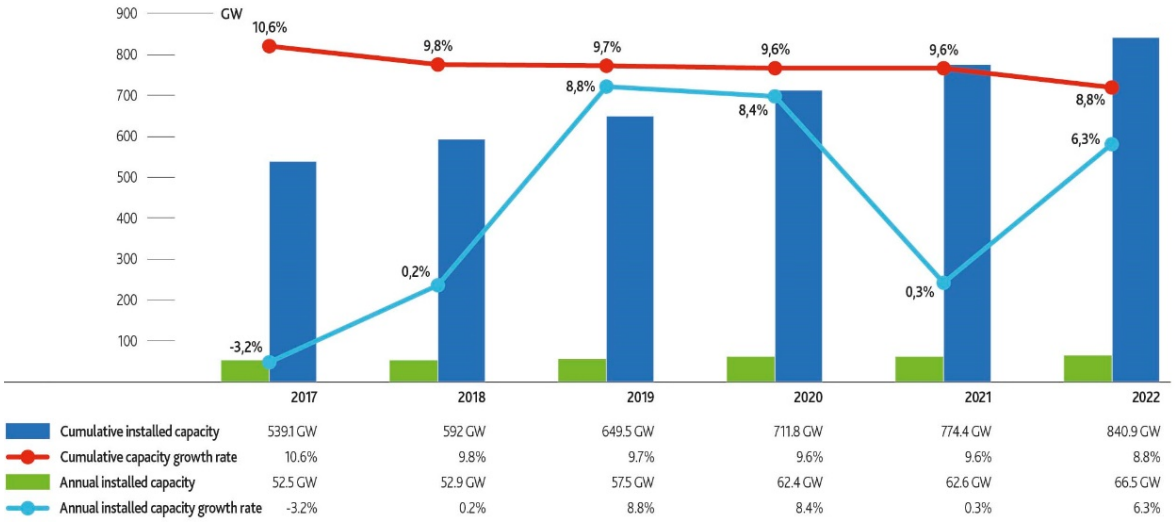

Figure 2.7. GWEC Forecasts for wind power capacity installments globally [30].

2.3. Wind Energy in Turkey

Turkish government agreed on a new policy in 2005 named Renewable Energy Law. The aim of this policy was to extend the contribution of renewable resources in electricity production, making them a part of the industry with safe, economical, and reliable means, to diversify the resource options, decrease greenhouse gas emission and protection of the environment [31]. It was the first regulation on licensing the renewable energy production facilities.

Turkey's yearly total wind power capacity and annual installations for 2007-2017 are shown in Figure 2.8 and Figure 2.9 [32]. Country's installed capacity was around 146 Megawatts in 2007 and it was about 6800 Megawatts as of 2017, it corresponds to 8% of all power.

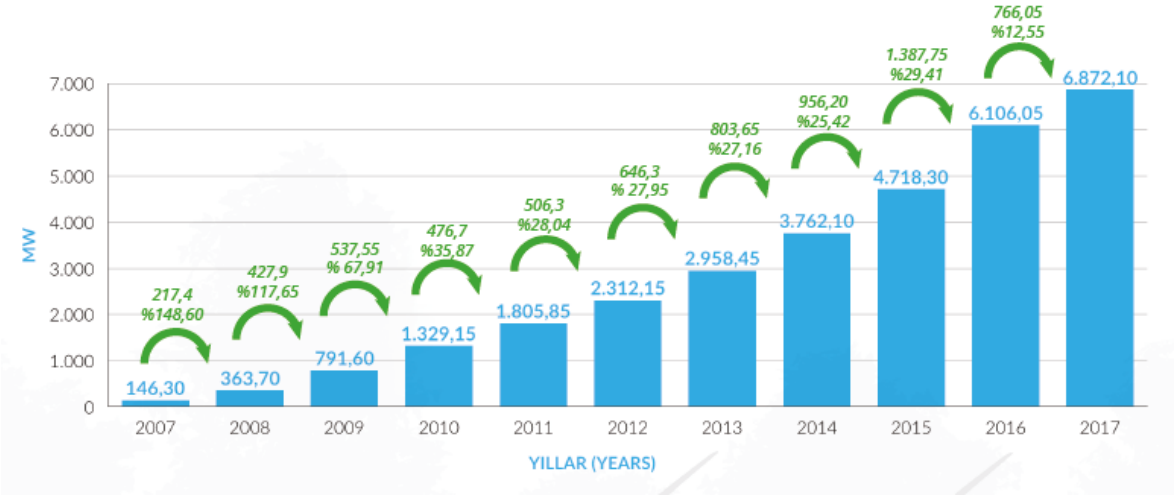

Figure 2.8. Cumulative Installations for Wind Power Plants in Turkey.

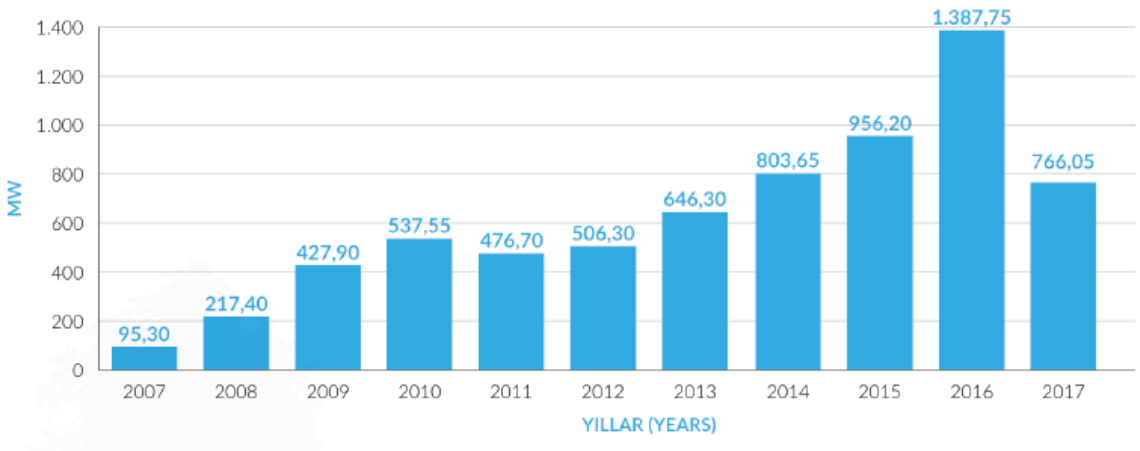

Figure 2.9. Annual Installations for Wind Power Plants in Turkey.

2.4. Seismicity in Turkey and Wind Power Plant Distribution

Turkey is located on an actively seismic zone. Several fault lines lie across the country and produce earthquakes frequently. This is due to constant move of Arabian plate to the north which results Anatolian Block's movement to the west. These plate movements created North Anatolian Fault and East Anatolian fault which produce earthquakes costing many lives and threatening the investments in the region. In addition to the North and East Anatolian faults, the Aegean region is seismically active due to the tectonic movements below and around the Aegean Sea. Between 1900 and 2012, 203 earthquakes having magnitude of M_w=6.0 or greater were recorded in Turkey and the surrounding region [33]. The 72 most destructive of them caused more than 90000 casualties and caused economic loss of and estimated USD 50 Billion to the Turkish economy. From 1992 onward, geological and seismological investigations on the earthquakes in Turkey have reasonably increased. 1999 Izmit (M_w=7.4) and 1999 Düzce (M_w=7.2) [34, 35], two of the most destructive earthquakes in the history of the country helped geoscientists to understand active faults.

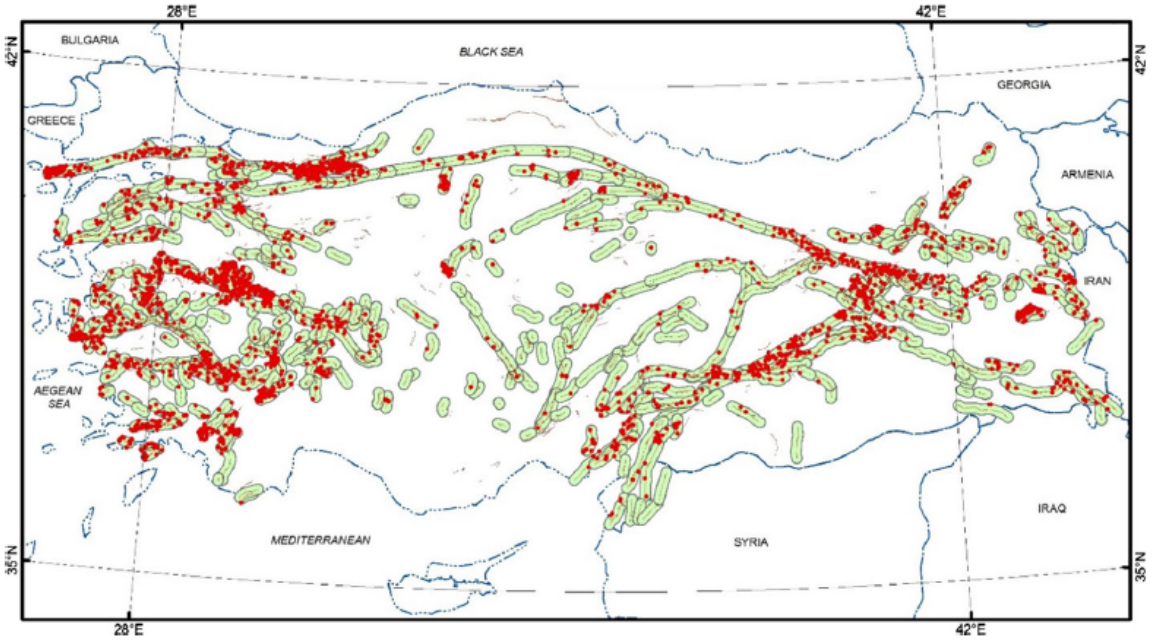

Figure 2.10. The Distribution of Earthquakes from 1900 to 2012 with $M_w > 4.0$ [36].

Figure 2.10 shows the earthquake events with $M_w > 4.0$ that took place between 1900 to 2012 in Turkey. It was prepared in 2016 [36] by examining 485 fault segments across the country.

These events increased the need and the effort for more detailed fault and seismic risk distribution maps across the country. AFAD, Turkish Disaster and Emergency Management Authority has released the up to date seismic hazard map in 2018 [37].

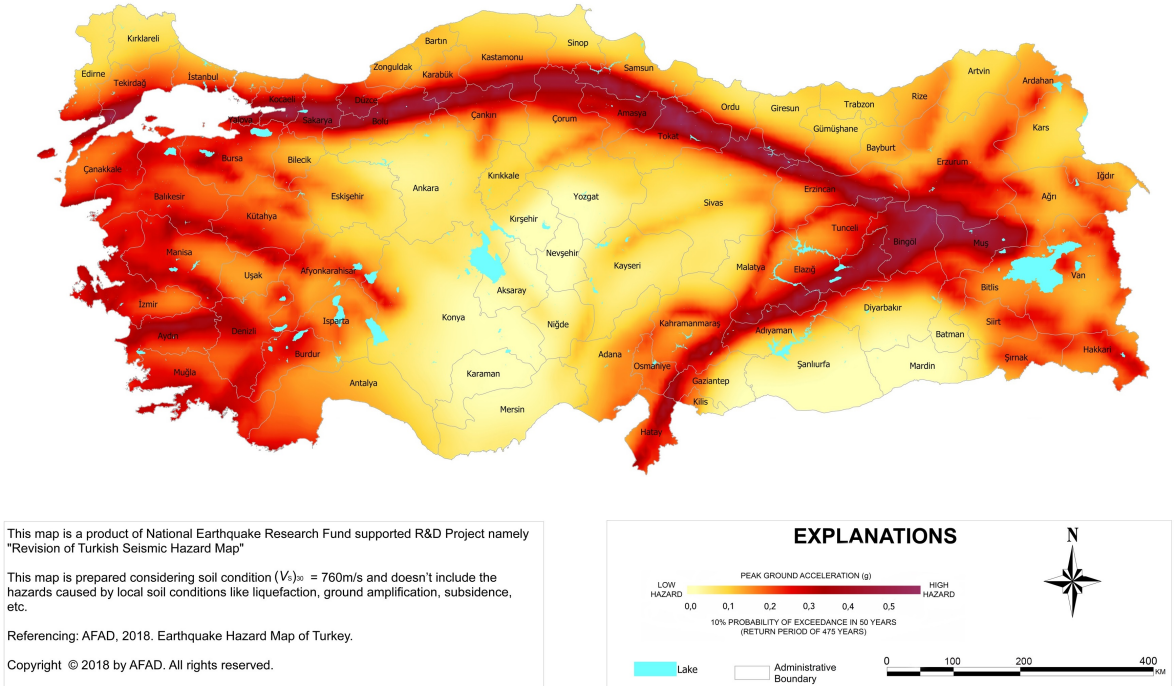

Figure 2.11. Earthquake Hazard Map of Turkey [37].

As shown in Figure 2.11, northern Anatolia and the southwest band and the Aegean region has the largest risk of facing with earthquake hazard.

With the light of the information on high seismicity of Turkey, the questions arise in terms of the "safety" of installments of any kind of industrial or energy generating facility including wind power plants on or near the seismically active zones. The locations of the wind turbines are chosen mainly according to wind capacity of the regions. Figure 2.12 shows the yearly average wind speed distribution at 100 meters height. It can be seen the majority of the wind potential is in the North Aegean Region and

the Marmara Region. This is the reason behind 34% of operational wind power plants being in Marmara Region and 39% being in Aegean region as of 2017 [32]. Figure 2.13 shows installed wind power plant capacities of every city. To harness the most out of the wind power, the investment is mostly done on the red zones of Figure 2.12. However, it should be noticed that most of the investment is in or near the red zones of Figure 2.11 as well. This should not stop the new investments in these regions but should be carefully monitored and seismic resistance should be implemented in the design and construction stages of wind turbine towers, foundations and when necessary piles.

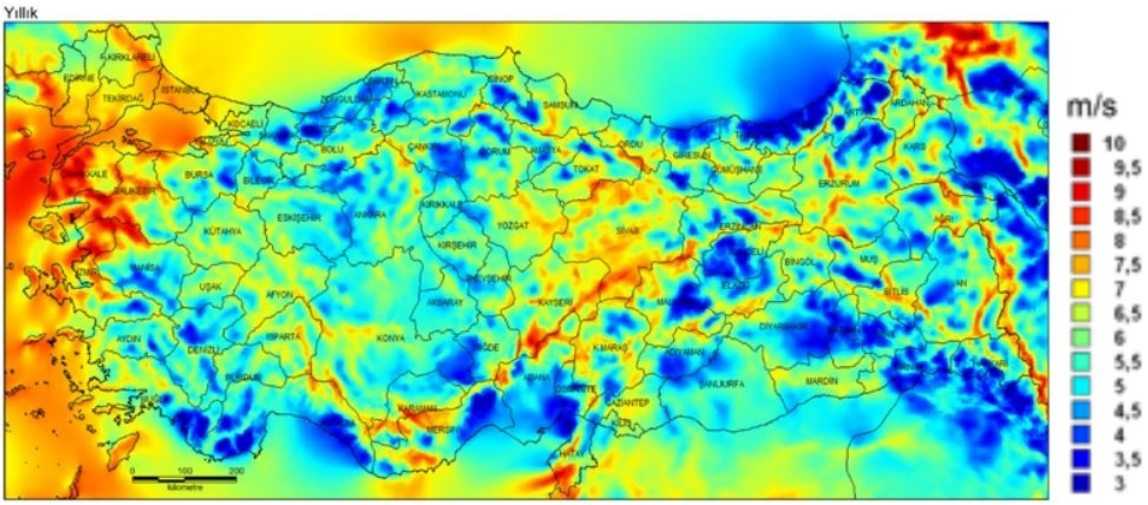

Figure 2.12. Yearly Average Wind Speed Map 100 Meters Above Ground [38].

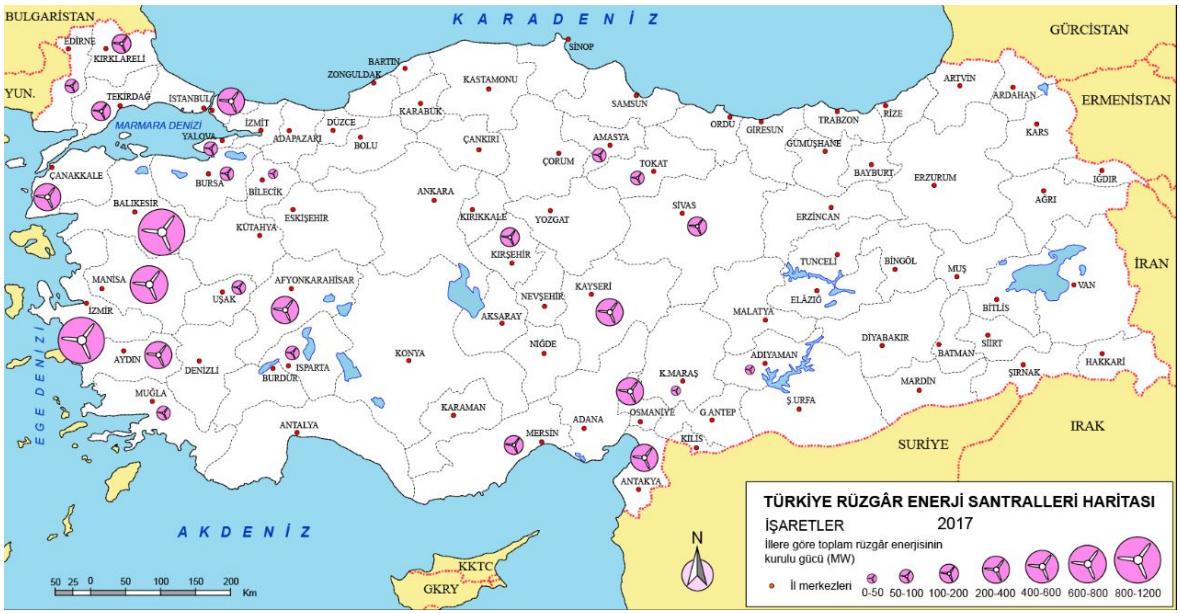

Figure 2.13. Installed Wind Power Plant Capacity of Cities of Turkey [39].

3. FINITE ELEMENT MODELLING

3.1. Details of the Modelled Wind Turbine

The wind turbine investigated in this work is a 900-kW model with a hub height of 54 meters and a rotor diameter of 44 meters. The turbine is in Boğaziçi University Sarıtepe Campus. It is located on soil with site conditions of top 10.5 meters from ground being sand and below that being silty clay. The drawings of the tower and the details about the weights and geometry of the turbine parts are taken from the manufacturing company's specification documents.

Figure 3.1. 900 kW Wind Turbine Subject of This Work.

Table 3.1. Soil Properties.

Soil Properties	**Sand (0 to -10.5 m)**	**Silty Clay (Below -10.5 m)**
Unit Weight (kN/m^3)	16	18
Cohesion (kPa)	0	66.6
Internal Friction Angle (degree)	22	9

Table 3.2. Turbine Structure Mechanical Properties.

Rated Power (kW)	900
Hub Height (m)	54
Rotor Diameter (m)	44
Nacelle + Rotor + Hub Mass (tons)	37
Steel Elasticity Modulus (MPa)	200
Steel Density (kg/m^3)	7850
Steel Yield Strength (MPa)	355

The thickness of the tower section varies over the height of tower from 24 mm on the base to 12 mm on top. The diameter of tower section is also varying from the base to the top from 3.3 m to 1.3 m giving the tower a tapered form. The tower has 3 parts connected to each other by bolts. The connections between tower parts were not modelled explicitly in the finite element models, but they were assumed as being continuous (fixed). The turbine has a pile group and cap as foundation. The design drawings show that there are 26 piles of 18-meter length. The pile plan is given in Figure 3.2.

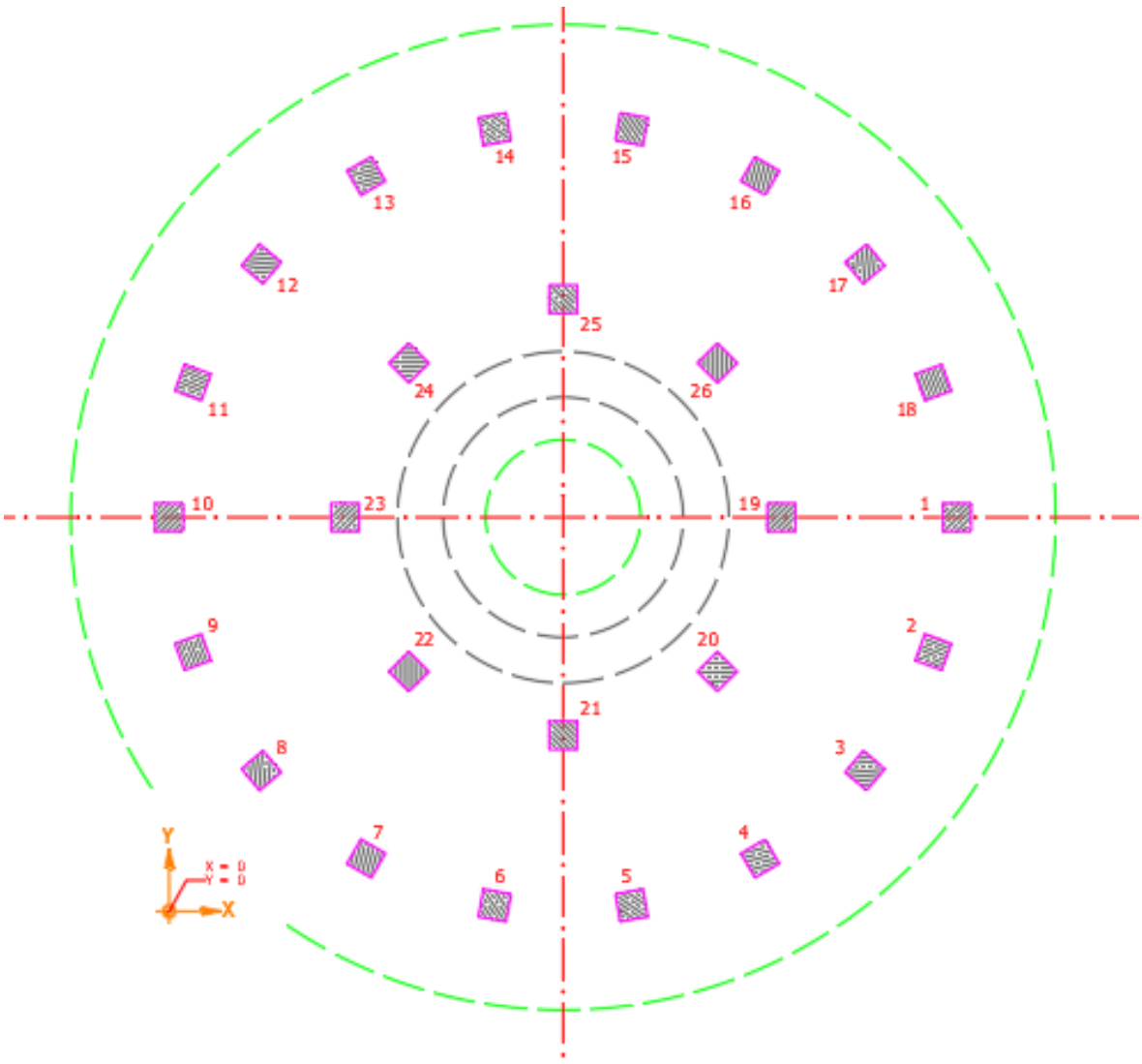

Figure 3.2. Pile Plan.

The pile plan shows two circular lines of piles with inner circle's radius being 3.1 m and outer circle's radius being 5.6 meters. The cap section is given in Figure 3.3.

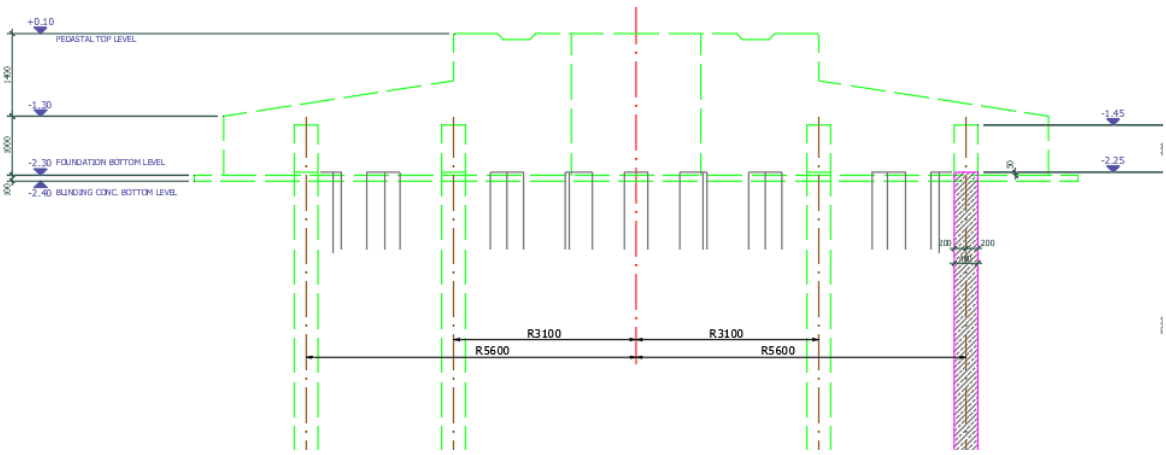

Figure 3.3. Foundation Section.

Due to the infeasibility of modelling the reinforcements of the piles and cap, they were modelled as elastic solid elements for the analyses. It should be noted that modelling these parts as elastic solids ignores the nonlinear behavior of concrete under tensile loads. The concrete classes for the parts are given in Table 3.3.

Table 3.3. Concrete Properties.

	Class	**Young's Modulus (GPa)**
Pile Concrete	C25/30	30
Cap Concrete	C35/45	33

3.2. Finite Element Models

This section describes the finite element models prepared for estimating the response of a wind turbine to earthquake motion. Three different models were prepared.

They are:

(i) Continuum Model
(ii) Global Spring Model
(iii) API Spring Model

Continuum model includes the 25 meters deep soil, 26 piles with cap and the 54 meters high steel tower. Global spring model consists of the tower with added base soil springs in translational and rotational degrees of freedom. API Spring model refers to the soil springs, piles, cap, and the tower model. It consists of so called p-y, t-z and q-z springs as defined in API guidelines [40]. p-y springs are nonlinear horizontal springs connected to the piles. t-z springs are vertical springs connected to the piles on the same nodes with p-y springs. q-z springs are vertical springs connected to pile tip. The constitutive relationships for these springs are defined in American Petroleum Institute Guidelines [40].

3.2.1. Continuum Model

The continuum model refers to the full model including soil, pile group, cap and tower explicitly. The soil material model was defined as SOLID186 elastic-perfectly plastic elements with mohr-coulomb failure criteria. The piles, cap and tower were modelled as SOLID186 with elastic solid elements. Mass of nacelle, rotor and hub were defined as a point mass by MASS21 element with eccentricity at top of the tower. The outer boundaries of soil were fixed against translation and rotation. A soil block of width 50 meters in both horizontal directions was defined to provide enough fading of the soil motion far from the structure. The contacts between soil and the pile foundation were defined as "frictional contacts" with CONTA174 elements. A Frictional contact is a nonlinear contact that is separable under tension, carries compressive stresses and provides sliding resistance between two contact surfaces by the defined friction coefficient. The friction angle between piles and soil from literature [41] was waken as 22 degrees. The friction coefficient between two surfaces being tangent of the friction angle, therefore 0.5.

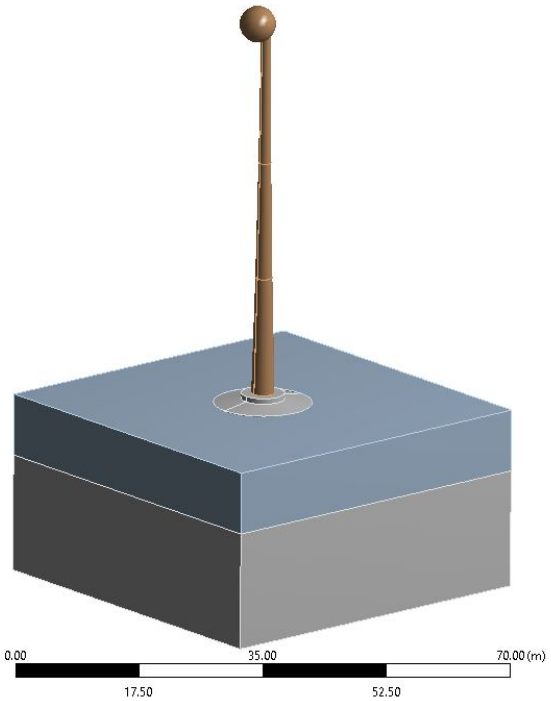

Figure 3.4. Continuum Model.

In addition to the soil nonlinearity and the contact nonlinearity between concrete and soil, the geometric nonlinearity meaning the second-degree effects from large deflections were also considered during analysis.

The soil properties as given in Table 3.1 were used. However, the Young's Modulus of the soil was unknown. To obtain the Young's Modulus, different E values were assigned to the soil and then the modal parameters of the numerical model were matched with the obtained mode frequencies from the FDD of ambient vibration responses of previously installed sensors on the structure. Mode shapes were also obtained.

FDD technique was proposed by Brincker in 2001 [42]. It is an output only system identification method.

Table 3.4 shows the varying young's modulus values assigned to soil and corresponding mode frequencies for each E value. The E value was taken same for both

Figure 3.5. Pile Group in the Model.

layers of soil and the range for the elasticity modulus was taken from literature [43]. Fore aft stands for the direction normal to the rotor and side to side refers to the parallel to ground direction perpendicular to fore aft.

Table 3.4. Soil Young's Modulus vs. Mode Frequencies.

	Fore Aft			Side to Side		
E (MPa)	1st Mode Frequency (Hz)	2nd Mode Frequency (Hz)	3rd Mode Frequency (Hz)	1st Mode Frequency (Hz)	2nd Mode Frequency (Hz)	3rd Mode Frequency (Hz)
1	0.36	2.15	6	0.36	2.15	6
5	0.45	2.95	6.7	0.45	2.99	7.5
10	0.46	3.22	7.5	0.47	3.27	8.2
15	0.47	3.33	7.8	0.47	3.38	8.6
20	0.47	3.39	8.1	0.47	3.45	8.9
25	0.48	3.43	8.2	0.48	3.49	9
30	0.48	3.46	8.3	0.48	3.52	9.1
50	0.48	3.52	8.5	0.48	3.58	9.4
Fixed	0.49	3.68	9	0.49	3.75	10

Ambient vibration responses of the wind turbine's tower were recorded with accelerometers. Then, FDD was used to obtain mode frequencies and mode shapes. Figure 3.6 shows the sensor layout on the structure, and their heights from the ground together with their orientations. Sensors are positioned on the inner walls of the tower. Sensors 2,4 and 10 were chosen since they are positioned along the height of the tower having same orientation. Figure 3.7 3.8 and 3.9 shows the acceleration records obtained from sensors 2, 4 and 10. Figure 3.10 shows the obtained mode frequencies by FDD. Figure 3.11 shows the identified mode shapes.

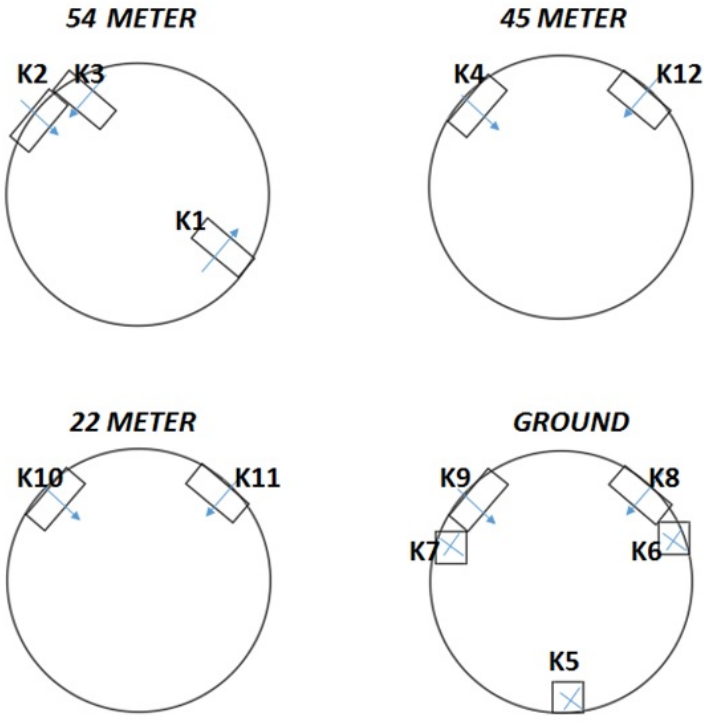

Figure 3.6. Sensor Layout.

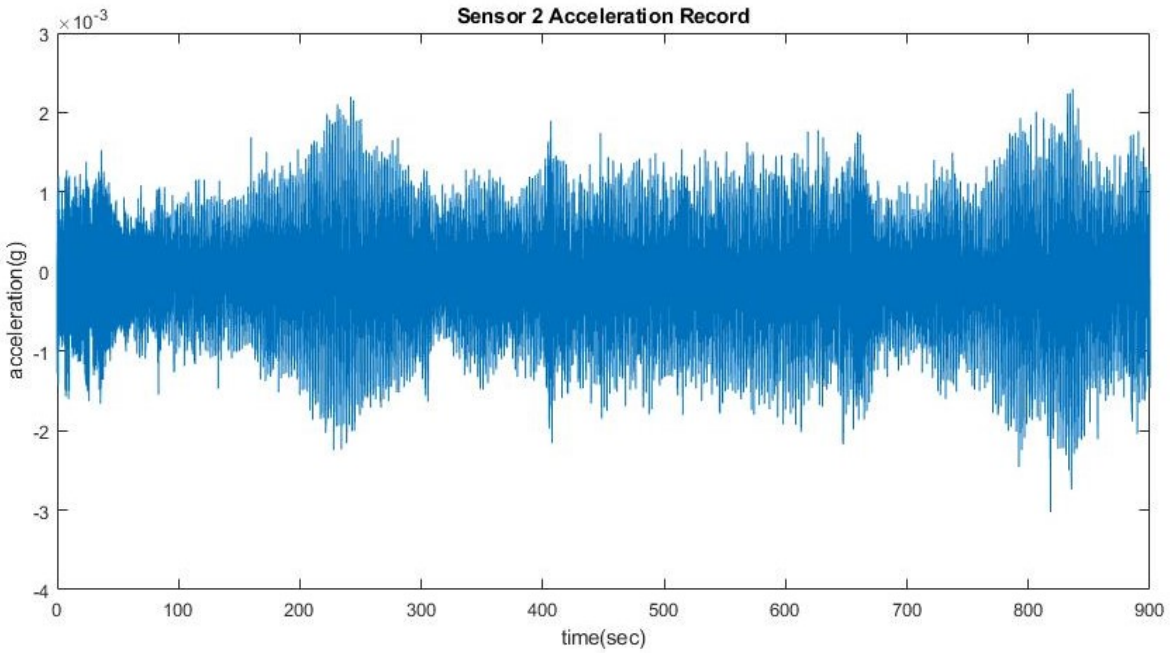

Figure 3.7. Acceleration Record from Sensor 2.

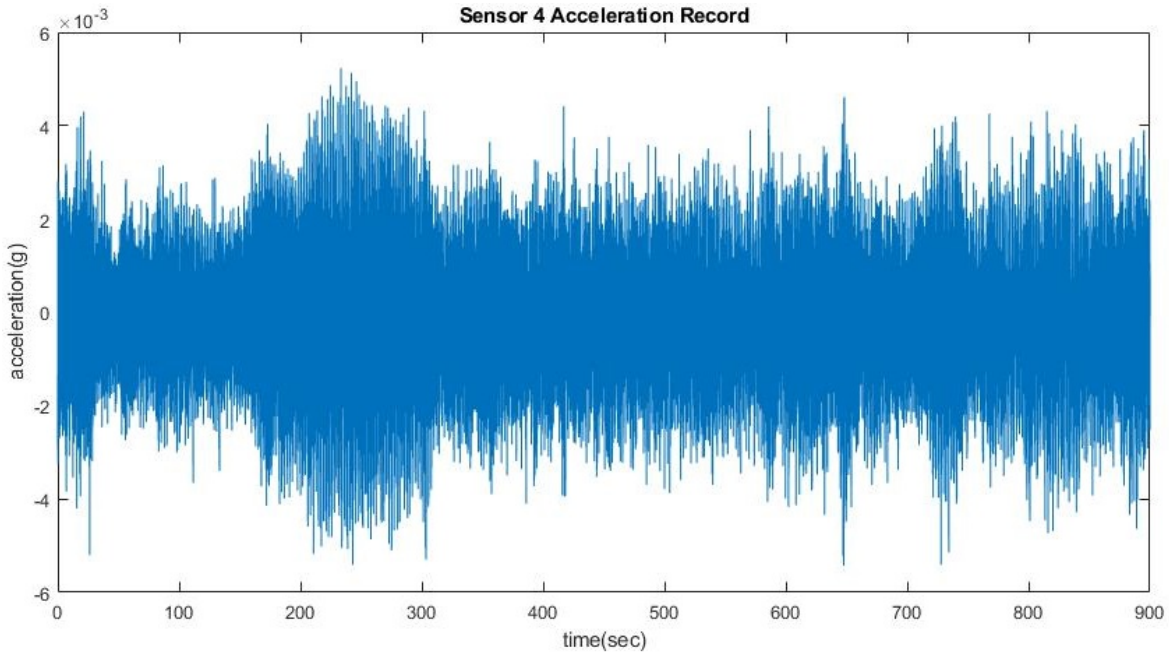

Figure 3.8. Acceleration Record from Sensor 4.

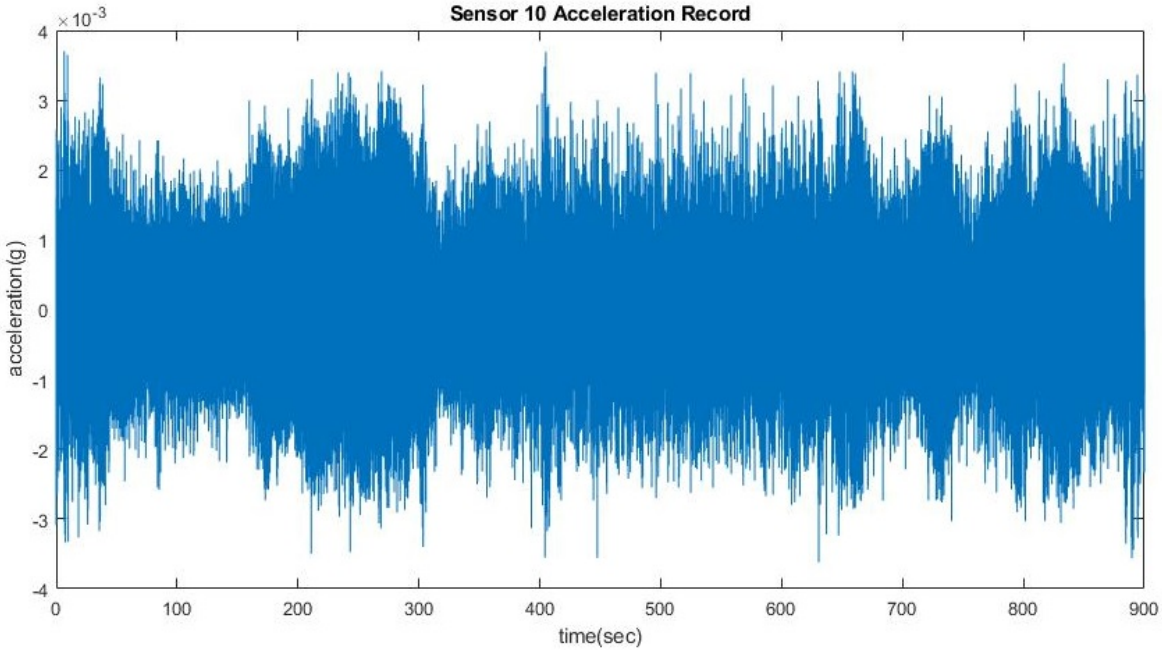

Figure 3.9. Acceleration Record from Sensor 10.

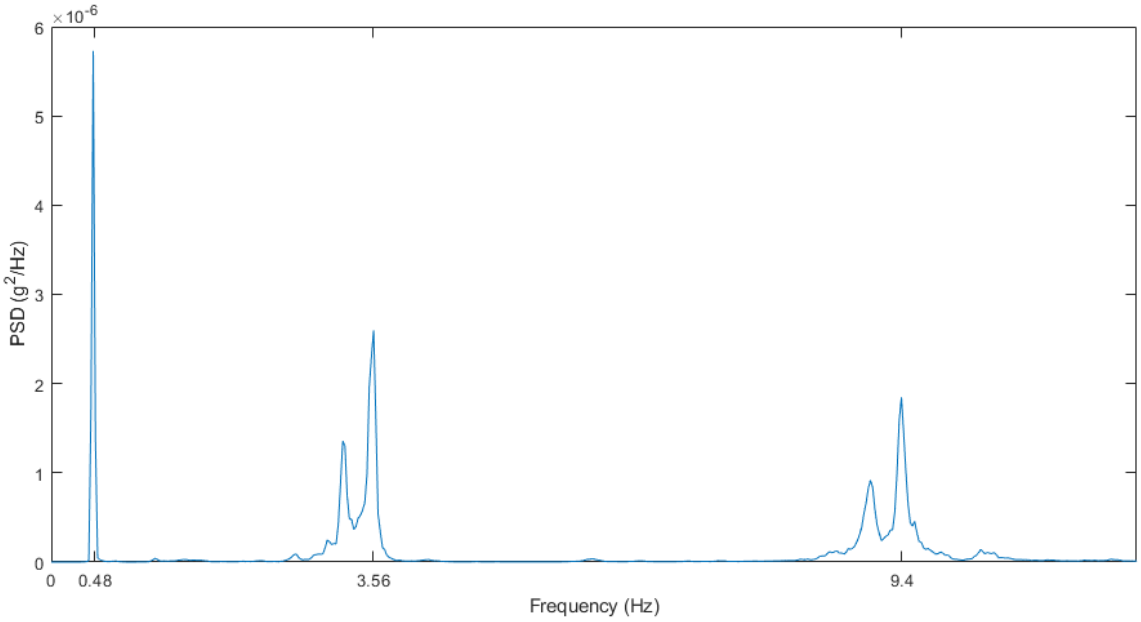

Figure 3.10. Power Spectral Density and Identified Mode Frequencies.

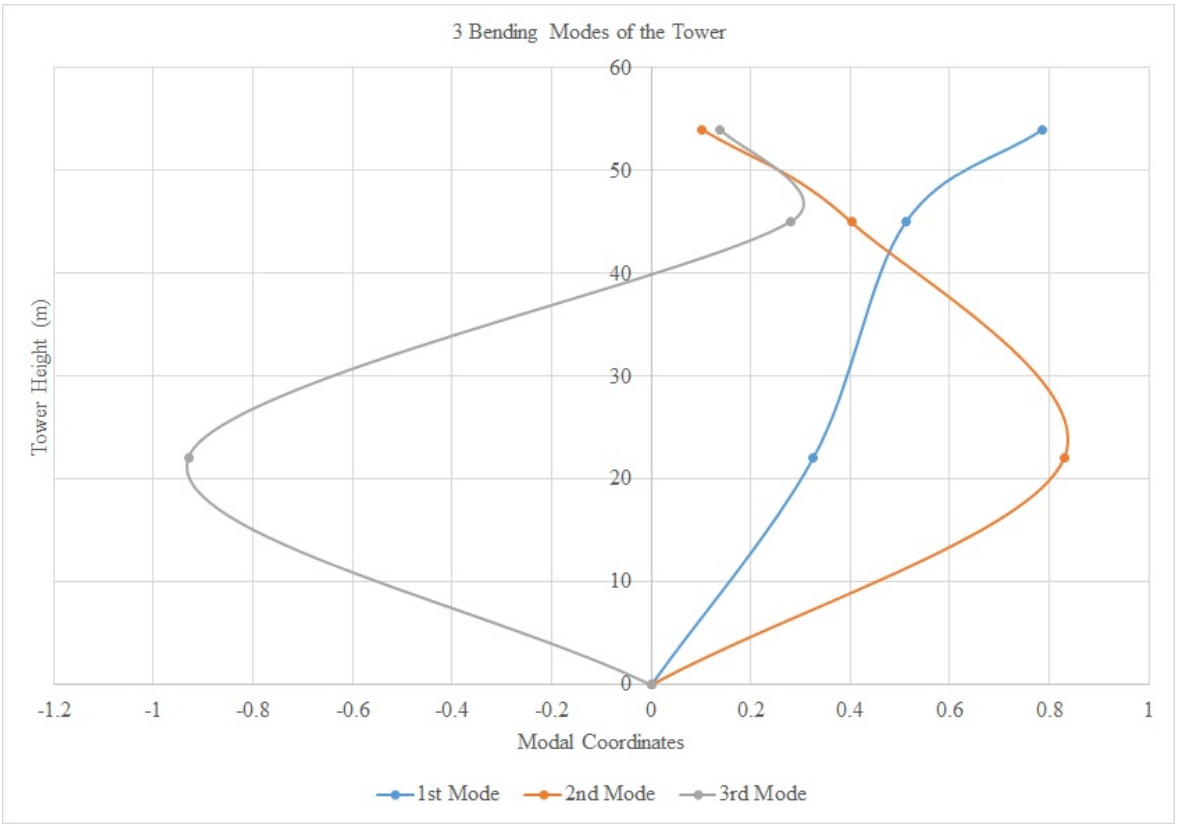

Figure 3.11. Identified Mode Shapes.

Table 3.5. Structural Mode Frequencies.

	1st Bending	2nd Bending	3rd Bending
Mode Frequency (Hz)	0.48	3.56	9.4

At this stage, it should be noted that the position of the blades at the time of acceleration records are unknown. This implies the peaks from the FDD of records are not necessarily fore aft or side to side. The smaller peaks next to the 2nd and 3rd mode peaks in Figure 3.10 are due to this uncertainty. Comparing the obtained frequencies from records with the modelled frequencies at Table 3.4, 50 MPa Young's modulus for the soil was chosen. This value was used as initial modulus for time history analyses to come. In addition, it was used for the Global Spring model to obtain spring stiffnesses as will be explained in the next section.

3.2.2. Global Spring Model

The process of developing the global spring model is as follows:

(i) Soil and pile group with massless and infinitely rigid cap were modelled without the tower. The difference from the continuum model is that tower not being included and the cap being rigid and massless.

(ii) Incremental static force was applied to the cap in two horizontal and the vertical directions. Incremental static moment was applied to the cap about two horizontal directions.

(iii) The force-displacement and moment-rotation relationships obtained by nonlinear static analyses were assigned to the nonlinear springs defined by COMBIN39 elements to be attached under the tower. The hysteresis behavior for nonlinear springs was defined such that unloading and reloading followed initial stifness slope.

As defined above, the tower was removed from the model and static loadings were applied to the cap. Then load displacement relationships were obtained to be used as backbone curves of global springs to be attached to tower base.

In the Figures 3.12, 3.13, 3.14, 3.15 and 3.16, the deformed shapes of the cap and soil as well as the load deformation relationships are given.

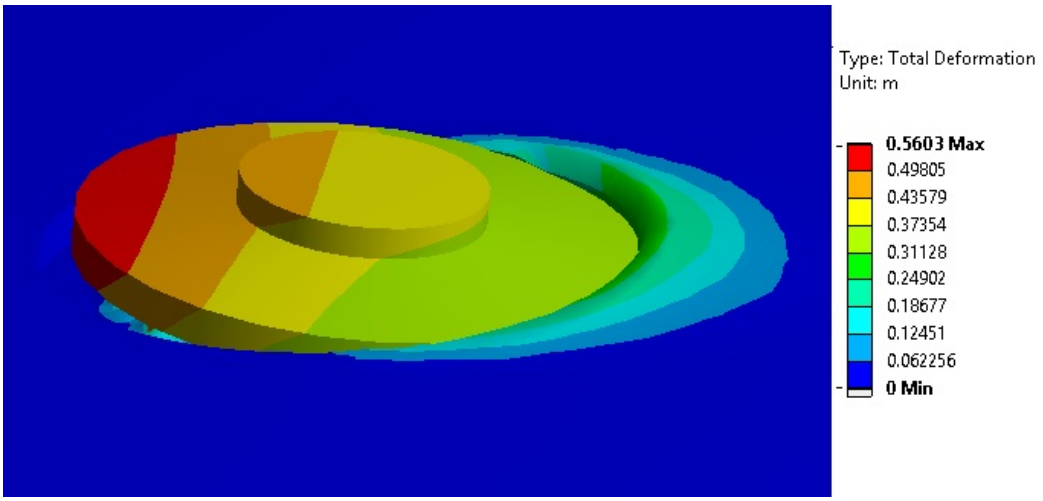

Figure 3.12. Deformed Shape of the Cap and Soil Under Incremental Static Lateral Force.

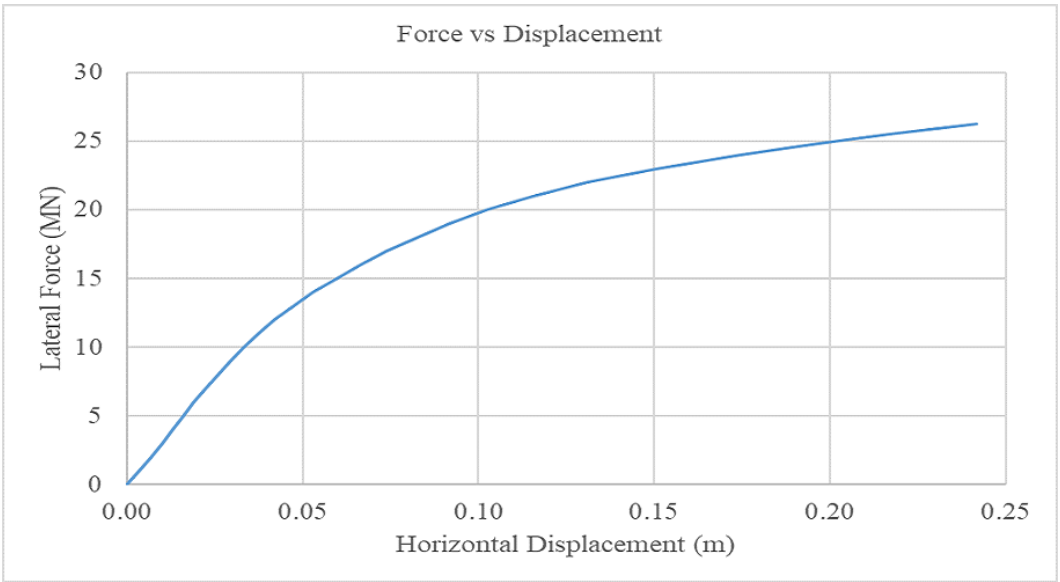

Figure 3.13. Lateral Force vs Cap Horizontal Displacement.

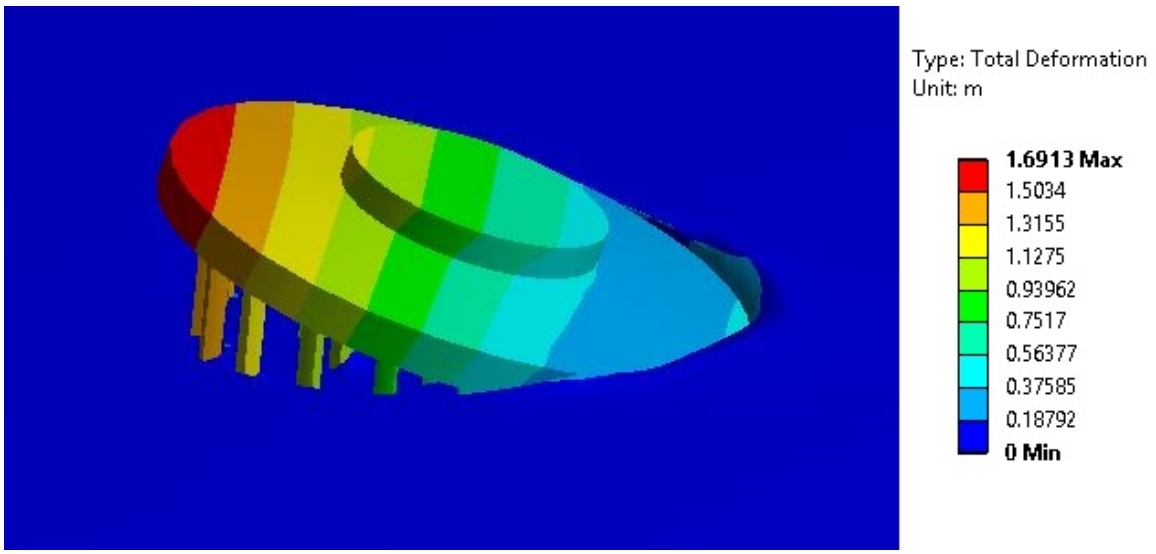

Figure 3.14. Deformed Shape of the Cap Under Incremental Static Moment.

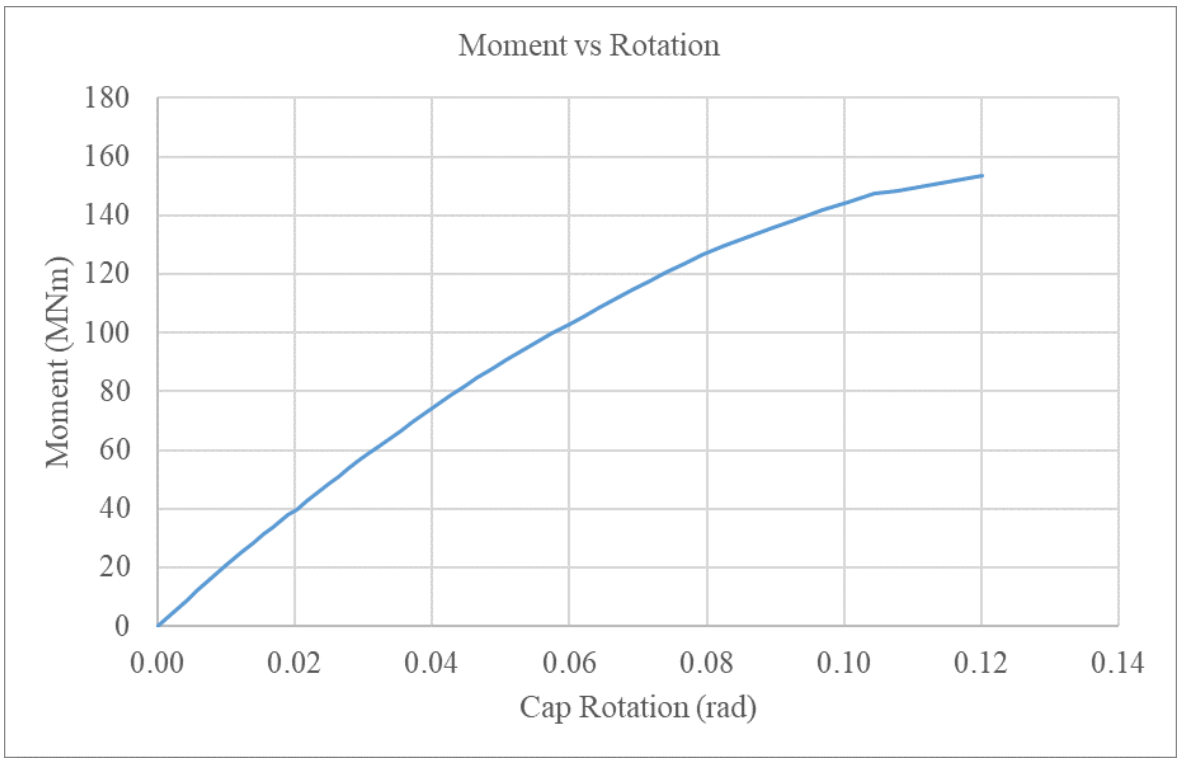

Figure 3.15. Moment Cap Rotation Relation.

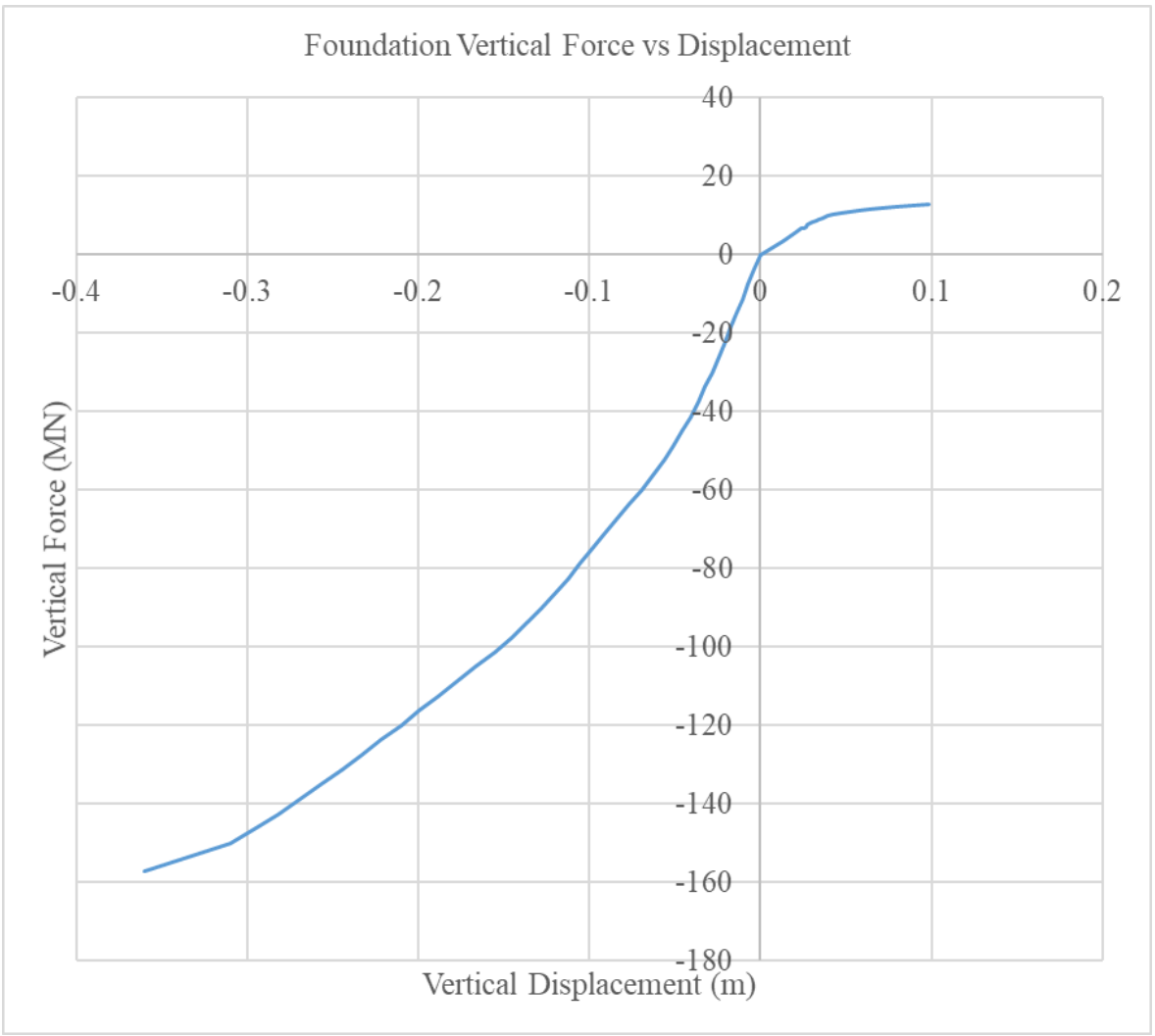

Figure 3.16. Vertical Force Cap Displacement Relation.

Figure 3.17. Tower with Global Springs.

The tower model with nonlinear springs attached to its base is shown in Figure 3.17. The model features 5 springs in total; two of which are rotational springs about horizontal directions perpendicular to each other, other two being translational springs along both horizontal direction and the fifth being the vertical spring. The hysteresis behaviour of the nonlinear springs were defined such that the unloading curve follows the same slope with initial stiffness. The visualization of the unloading path is shown in Figure 3.18 with solid lines following dashed lines with same slope of the curve at origin.

The length of the springs in ANSYS software do not add any attribute. They are just for visualization purposes.

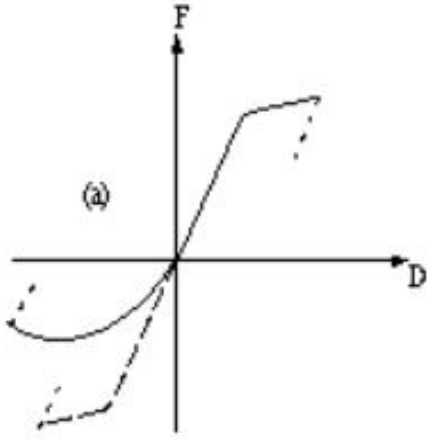

Figure 3.18. Nonlinear Spring Loading-Unloading Path [44].

3.2.3. API Springs Model

The third model created included the tower, foundation cap, pile group and nonlinear longitudinal soil springs in vertical and horizontal directions attached to the piles with a spacing of 1.5 meters. Solids were modelled with SOLID186 elements and springs were modelled with COMBIN39 elements. Soil springs were attached to the piles on one side and were fixed on the other side. The force displacement relationships for soil springs were created following API Guidelines. The only material nonlinearity was due to springs. The geometric nonlinearity from second degree effects were again considered.

A p-y curve defines the lateral soil resistance-deflection relationship. API guideline provides p-y soil spring formulations for sand referring to the literature from O'Neill and Murchinson (1983) [45] and for clay from Matlock (1970), and Reese and Cox (1975) [46, 47]. The suggested spring load deformation curve shapes are provided for each type of soil in the guideline. Depending on the soil properties, the ultimate resistance of the soil spring is calculated by empirical equations and then the path to the ultimate loads are followed from guideline.

- py springs for sand:

  The lateral soil resistance-deflection (p-y) relationship for sand follows the equation below:

$$P = A \times p_{\mathrm{u}} \times tanh\left(\frac{k \times H}{A \times p_{\mathrm{u}}} \times y\right) \tag{3.1}$$

  where;

  H= Depth below ground (m).

  A= Factor to account for static or cyclic analysis, 0.9 for cyclic.

  p_{u} = Ultimate bearing capacity at depth H. Determined by taking the smallest of Equations 3.2 and 3.3 (kN/m).

  k= Initial bearing capacity at depth H. Determined by charts in guideline as a function of internal friction angle (kN/m^3).

  y= Lateral deflection.

$$p_{\mathrm{us}} = (C_1 \times H + C_2 \times D) \times \gamma \times H \tag{3.2}$$

$$p_{\mathrm{ud}} = C_3 \times D \times \gamma \times H \tag{3.3}$$

  where;

  D= Pile diameter. Taken as the diameter giving the same cross sectional area with square pile section (m).

  p_{u} = Ultimate resistance (s=shallow, d=deep) (kPa).

  γ= Effective soil weight (kN/m^3).

  C_1, C_2, C_3 = Coefficients determined by guideline charts as a function of internal friction angle.

- py springs for clay:

  The lateral soil resistance-deflection curve (p-y) for clay under cyclic loading has the coordinates given below:

Table 3.6. Clay p-y Curve Coordinates.

$X > X_R$		$X < X_R$	
$\frac{p}{p_u}$	$\frac{y}{y_c}$	$\frac{p}{p_u}$	$\frac{y}{y_c}$
0.00	0.0	0.00	0.0
0.50	1.0	0.50	1.0
0.72	3.0	0.72	3.0
0.72	∞	$0.72\frac{X}{X_R}$	15.0
		$0.72\frac{X}{X_R}$	15.0

where;

X = Depth below soil surface.

X_R= Depth below soil surface to bottom of reduced resistance zone. Given by:

$$X_R = \frac{6D}{\frac{\gamma D}{c} + J}$$

c = Undrained shear strength for undisturbed clay soil samples (kPa).

J = dimensionless empirical constant taken as 0.5.

y = Actual lateral deflection (mm).

$y_c = 2.5\varepsilon_c D$ (mm)

ε_c = Strain which occurs at one-half the maximum stress on laboratory undrained compression tests of undisturbed soil samples.

p = Actual lateral resistance (kPa).

where;

$$p_u = 3c + \gamma X + J\frac{cX}{D} \qquad for X < X_R$$

$$p_u = 9c \qquad for X > X_R$$

- tz curves for sands and clays:

  A t-z curve defines the relationship between axial load transfer and axial pile deflection at any depth on pile. The referred literature for t-z curves is from Kraft *et al.* [48].

  The axial soil resistance pile deflection curve (t-z) for sand has the coordinates given below:

Table 3.7. Sand t-z Curve Coordinates.

Sands	
$z(mm)$	$\frac{t}{t_{max}}$
0.00	0.00
2.54	1.00
∞	1.00

where;

z=Local pile deflection.

t= Mobilized soil pile adhesion (kPa).

t_{max} = Maximum soil pile adhesion or unit skin friction capacity taken as 67 kPa from guideline charts.

The axial soil resistance pile deflection curve (t-z) for clay has the coordinates given below:

where;

t_{max}= Maximum skin friction given by: $t_{max} = \alpha c$

$$\alpha = 0.5 \left(\frac{c}{p_o}\right)^{-0.5} \qquad for \frac{c}{p_o} < 1.0$$

$$\alpha = 0.5 \left(\frac{c}{p_o}\right)^{-0.25} \qquad for \frac{c}{p_o} > 1.0$$

p_o = Effective overburden pressure at the point in question (kPa).

Table 3.8. Clay t-z Curve Coordinates.

Clays	
$\frac{z}{D}$	$\frac{t}{t_{max}}$
0.0016	0.30
0.0031	0.50
0.0057	0.75
0.0080	0.90
0.0100	1.00
0.0200	0.90
∞	0.90

- tz curves for sands and clays:

  A q-z curve defines the mobilized end bearing resistance and axial pile tip deflection. The referred literature for q-z curves is from Kraft *et al.* [48]. The curve coordinates are the same for both sands and clays as given below. The difference is in total end bearing Q_p.

Table 3.9. Clay t-z Curve Coordinates.

q-z Curves	
$\frac{z}{D}$	$\frac{Q}{Q_p}$
0.002	0.25
0.013	0.50
0.042	0.75
0.073	0.90
0.1	1.00

where;

Q= Mobilized end bearing capacity.

Q_p= Total end bearing. given by $Q_p = qA_p$

A_p = Gross end area of pile (m^2).

q = Unit end bearing. Given by $q = 9c$ for clays and $q = p_o N_q$ for sands.

N_q = Dimensionless bearing capacity factor. Taken as 12 from charts in guideline.

Figure 3.19. API Springs Model.

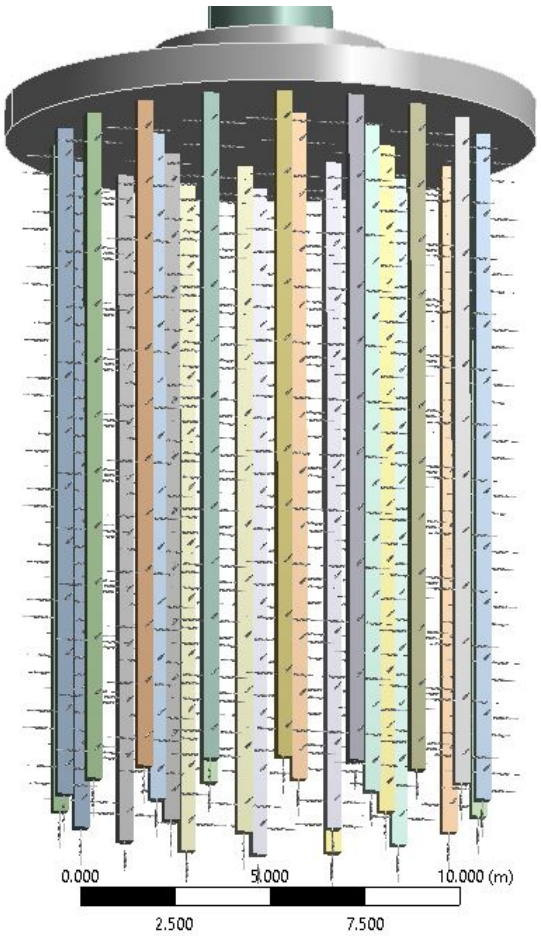

Figure 3.20. Close View of API Springs and Piles.

4. SEISMIC LOADING AND FRAGILITY ANALYSIS

4.1. Earthquake Selection Procedure

For the process of earthquake selection, Turkish seismic design code (2018) [49] was followed. Three component ground motions were chosen to be input. The procedure can be outlined as in following paragraphs.

First step was constructing the design response spectrum for the specific site. To do this, several site-specific properties had to be determined. It was achieved using the detailed earthquake risk map and active fault map of Turkey developed by AFAD [37] with selection of PGA mappings for an earthquake with return period of 475 years.

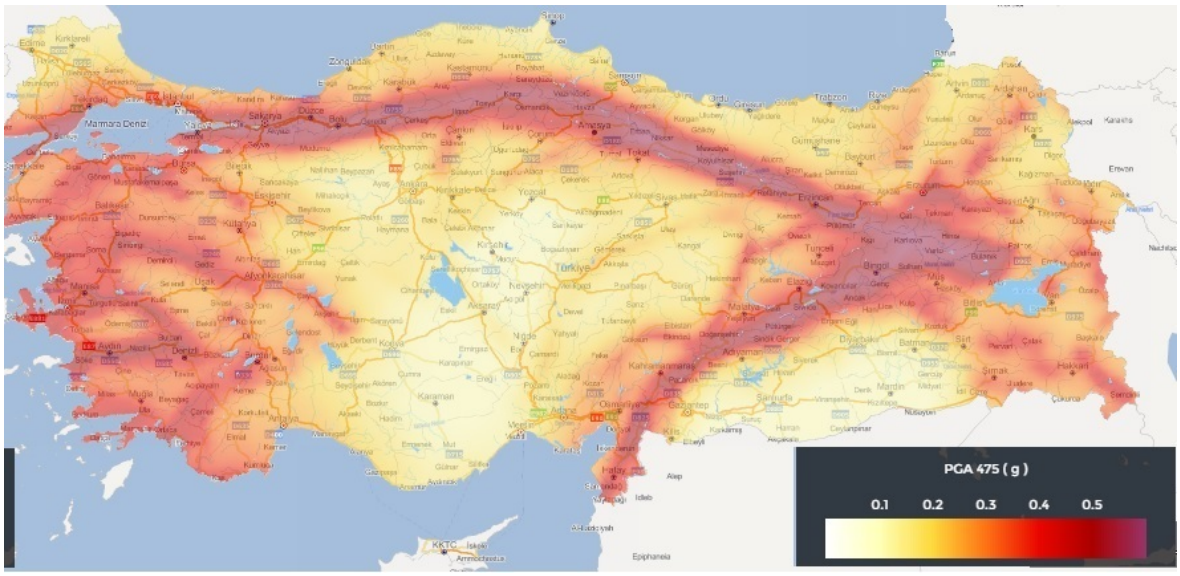

Figure 4.1. Earthquake Hazard Map for an Event with Return Period of 475 Years

Figure 4.2. Active Faults Around the Site and Site Location [37].

The design earthquake response spectrum equations in accordance with TBDY were developed as follows:

$$S_{\mathrm{DS}} = S_{\mathrm{S}} F_{\mathrm{S}} \tag{4.1}$$

$$S_{\mathrm{D1}} = S_1 F_1 \tag{4.2}$$

$$S_{\mathrm{ae}}(T) = \left(0.4 + 0.6\frac{T}{T_{\mathrm{A}}}\right) S_{\mathrm{DS}} \qquad (0 \leq T \leq T_{\mathrm{A}}) \tag{4.3}$$

$$S_{\mathrm{ae}}(T) = S_{\mathrm{DS}} \qquad (T_{\mathrm{A}} \leq T \leq T_{\mathrm{B}}) \tag{4.4}$$

$$S_{\mathrm{ae}}(T) = \frac{S_{\mathrm{D1}}}{T} \qquad (T_{\mathrm{B}} \leq T \leq T_{\mathrm{L}}) \tag{4.5}$$

$$S_{\mathrm{ae}}(T) = \frac{S_{\mathrm{D1}} T_{\mathrm{L}}}{T^2} \qquad (T_{\mathrm{L}} \leq T) \tag{4.6}$$

$$T_{\mathrm{A}} = 0.2\frac{S_{\mathrm{D1}}}{S_{\mathrm{DS}}} \tag{4.7}$$

$$T_{\mathrm{B}} = \frac{S_{\mathrm{D1}}}{S_{\mathrm{DS}}} \tag{4.8}$$

$$T_{\mathrm{L}} = 6s. \tag{4.9}$$

where;

S_{S}: Short period spectral acceleration from the PGA map.

S_1: 1 second period spectral acceleration from PGA map.

F_{S}: Seismic site coefficient for short period region.

F_1: Seismic site coefficient for 1 second period region.

S_{D1}: 1 second period design spectral acceleration.

S_{DS}: Short period design spectral acceleration.

T: Natural period of vibration of the structure.

T_A: Horizontal design spectrum corner period.

T_B: Horizontal design spectrum corner period.

T_L: Horizontal design spectrum transition period to constant displacement zone.

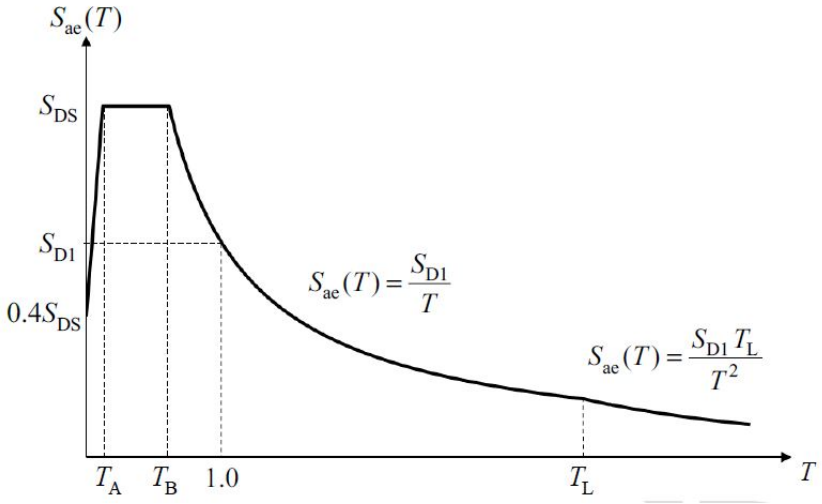

Figure 4.3. Horizontal Design Spectrum from TBDY.

The site-specific conditions for the analyzed wind turbine tower structure are defined in Table 4.1.

Table 4.1. Locational Details.

Coordinates		Site Details		Design Spectrum Parameters			
Longitude	Latitude	Site Class	L_F (km)	F_S	F_1	S_S (g)	S_1 (g)
29.01	41.24	ZD	41	1.4	2.2	0.57	0.17

The constructed design spectrum in accordance with the guidelines and with previously defined site parameters is given in Figure 4.4.

After constructing the design response spectrum, a specific region of structural periods was defined with bounds of $0.2T_1$ and $1.5T_1$ where;

T_1: Fundamental natural period of vibration of the structure.

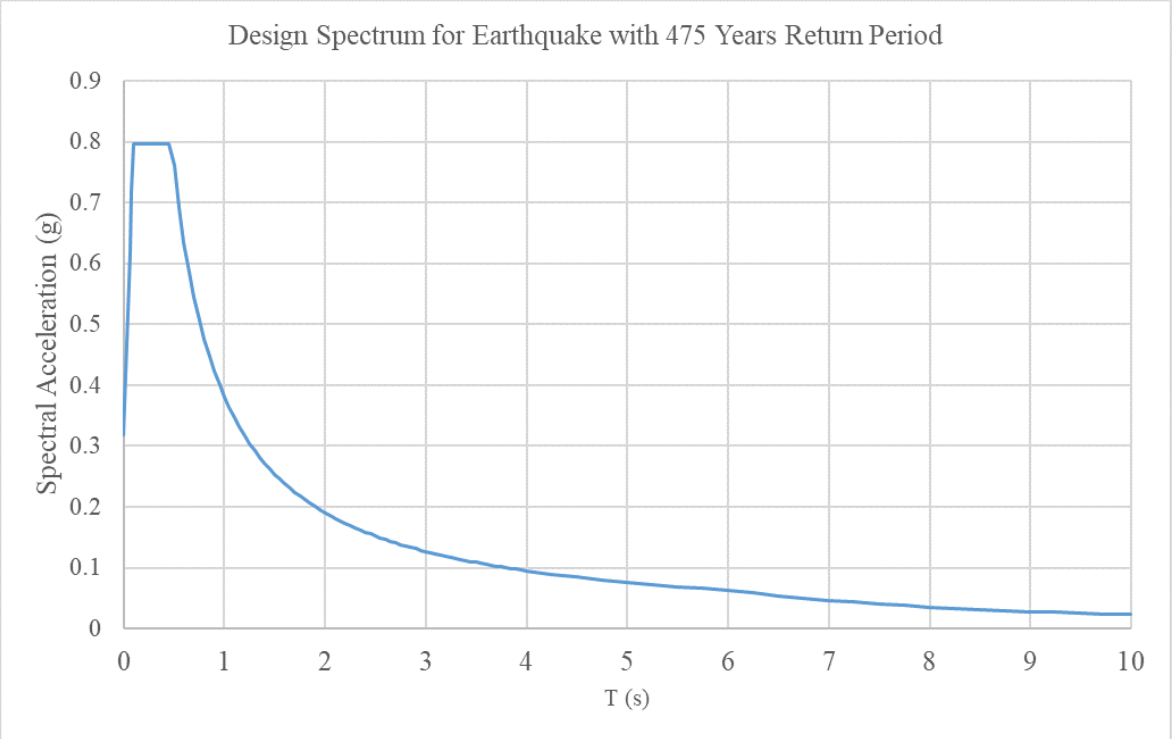

Figure 4.4. Constructed Horizontal Design Spectrum.

The first mode frequency of the wind turbine tower was given in Chapter 3 as $f_1 = 0.46Hz$.

$$T = \frac{1}{f} \tag{4.10}$$

Equation 4.10 gives $T_1 = 2.17s$. The range of interest for natural periods for ground motion selection is then from $0.2T_1 = 0.43s$. to $1.5T_1 = 3.26s$. The condition of choosing a time history fitting this design spectrum specific to the site in accordance with the seismic guideline is that, SRSS of the spectral response for the selected ground motion's two horizontal components or the average of SRSS of the selected multiple records' two horizontal components in the range of interest shall not be less than 1.3 times the design spectral responses in that range. Scaling of the ground motion time

history is possible.

In a similar manner to the horizontal components, the vertical design spectrum can also be constructed in accordance with the guidelines. The condition to choose the correct earthquake is such that the response spectral acceleration values for vertical component of the record shall not be less than those of vertical design spectrum. Scaling of the earthquake time history record is possible. Unlike the horizontal counterpart, multiplication of the design spectrum by 1.3 is not required. The procedure for constructing vertical design response spectrum and used equations are outlined below.

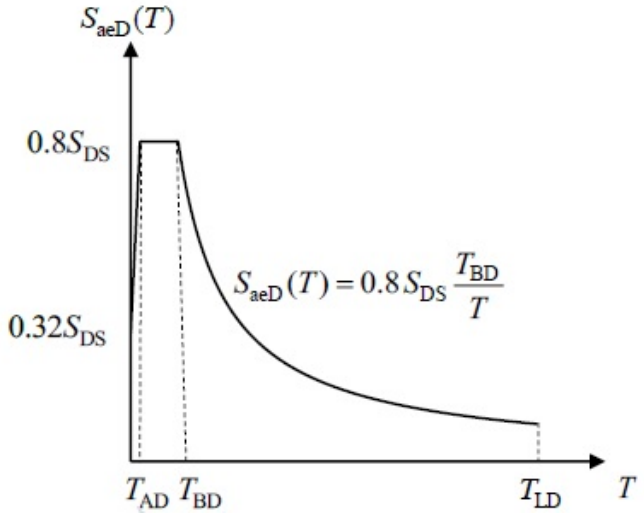

Figure 4.5. Vertical Design Spectrum from TBDY.

$$S_{\mathrm{aeD}}(T) = \left(0.32 + 0.48\frac{T}{T_{\mathrm{AD}}}\right) S_{\mathrm{DS}} \qquad (0 \le T \le T_{\mathrm{AD}}) \tag{4.11}$$

$$S_{\mathrm{aeD}}(T) = 0.8 S_{\mathrm{DS}} \qquad (T_{\mathrm{AD}} \le T \le T_{\mathrm{BD}}) \tag{4.12}$$

$$S_{\mathrm{aeD}}(T) = 0.8 S_{\mathrm{DS}} \frac{T_{\mathrm{BD}}}{T} \qquad (T_{\mathrm{BD}} \leq T \leq T_{\mathrm{LD}}) \tag{4.13}$$

$$T_{\mathrm{AD}} = \frac{T_{\mathrm{A}}}{3} \tag{4.14}$$

$$T_{\mathrm{BD}} = \frac{T_{\mathrm{B}}}{3} \tag{4.15}$$

$$T_{\mathrm{LD}} = \frac{T_{\mathrm{L}}}{2} \tag{4.16}$$

Where,

T_{AD}: Vertical design spectrum corner period.

T_{BD}: Vertical design spectrum corner period.

T_{LD}: Vertical design spectrum transition period to constant displacement zone.

The constructed design spectrum for vertical component is given in Figure 4.6.

With the light of the information given so far, PEER database was scanned to find ground motion records conforming to the criteria. Both horizontal and vertical

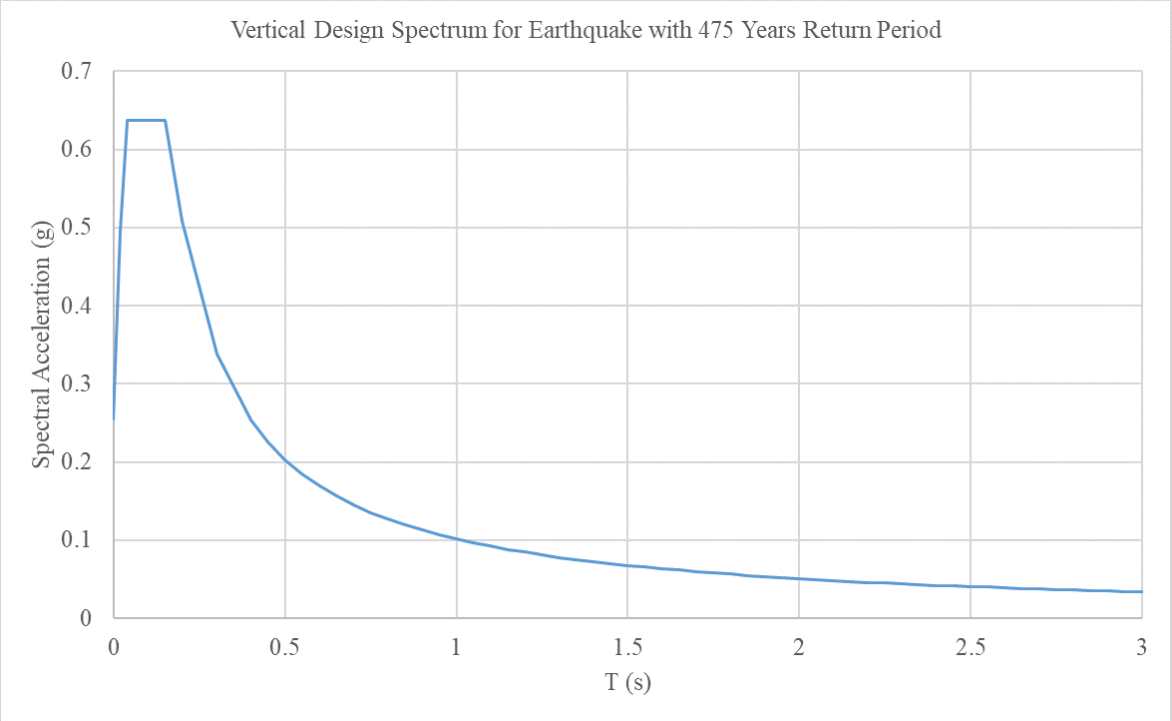

Figure 4.6. Constructed Vertical Design Spectrum.

components were checked to be fitting to the specifications of the guidelines. The chosen ground motion records and their response spectra are given in Table 4.2 and Figures 4.7 and 4.8.

Table 4.2. Chosen Ground Motion Records.

RSN #	Event Name	Scale Number	Horizontal SRSS PGA (g)	Vertical PGA (g)
764	Loma Prieta (1989)	1.6	0.48	0.24
1158	Kocaeli (1999)	1.0	0.40	0.20
6927	Darfield (2010)	1.0	0.49	0.91

As seen in Figure 4.7. The mean of the SRSS of the selected records' horizontal component response spectra in the range of interest exceed the target. The target was defined as 1.3 times the design response spectrum as mentioned earlier.

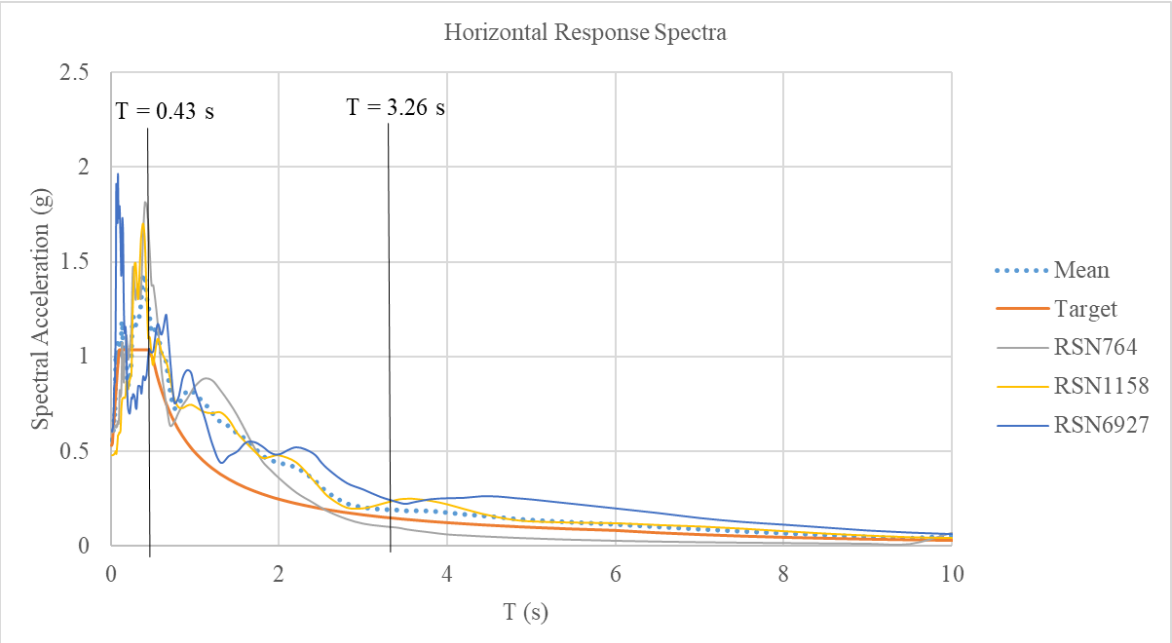

Figure 4.7. Horizontal Response Spectra of Selected Ground Motion Records.

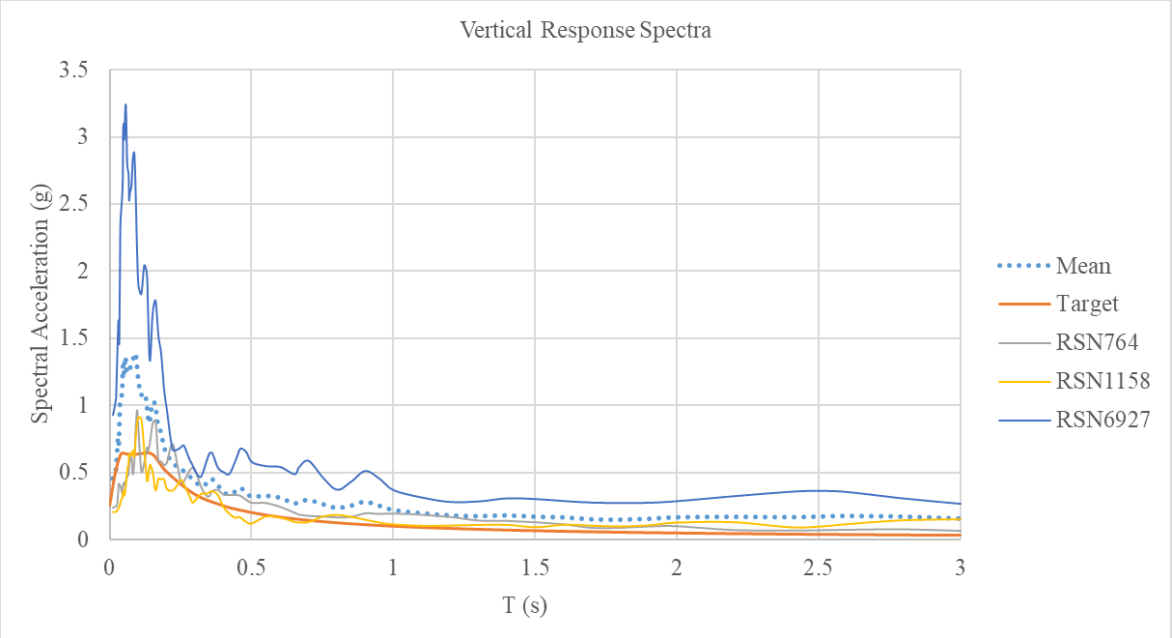

Figure 4.8. Vertical Response Spectra of Selected Ground Motion Records.

As seen in Figure 4.8, mean of response spectra of all chosen ground motions' vertical component fall above the target design spectra.

4.2. Comparison of Three Finite Element Models

The purpose of developing three different finite element models was to compare each of them and have an idea about accuracy and feasibility of each. The accuracy is not straightforward to achieve or assess since unfortunately there are no earthquake records caught so far by the instrumented accelerometers. But still one can compare the modal properties from system identification with the numerical models.

The feasibility of the methods can be assessed by the time it takes to create the models and by the time it takes to perform the analyses. Even though nowadays powerful computers and workstations are common comparing to decades ago, still fine detailed numerical models can yield considerably long analysis durations and convergence issues.

Firstly, to compare the accuracy of the model, the identified structural mode frequencies were compared with those obtained from finite element models. As shown in Tables 4.3 and 4.4, all three models resulted with mode frequencies close to identified values. The first mode frequency was found to be more sensitive to the point mass at the top of the tower rather than soil stiffness. The second mode frequency was the most sensitive to changes in soil stiffness values.

After comparing the modal values, Kocaeli event ground motion record was applied to three models and the top displacements were compared. They are shown in Figures 4.9 and 4.10

As seen in the plots, the maximum responses of top displacement from three models do not differ significantly. One can note that the three responses are noticed to be not completely in phase. However, since the total lateral top displacement values (SRSS of both components) are close to each other as in Table 4.5, the three models

Table 4.3. Model Mode Frequencies.

	Fore Aft			Side to Side		
	1st Mode Frequency (Hz)	2nd Mode Frequency (Hz)	3rd Mode Frequency (Hz)	1st Mode Frequency (Hz)	2nd Mode Frequency (Hz)	3rd Mode Frequency (Hz)
Continuum	0.48	3.52	8.5	0.48	3.58	9.4
Global Springs	0.48	3.54	8.6	0.48	3.60	9.5
API Springs	0.47	3.56	8.3	0.47	3.63	8.8

Table 4.4. Identified Mode Frequencies.

	1st Bending	2nd Bending	3rd Bending
Mode Frequency (Hz)	0.48	3.56	9.4

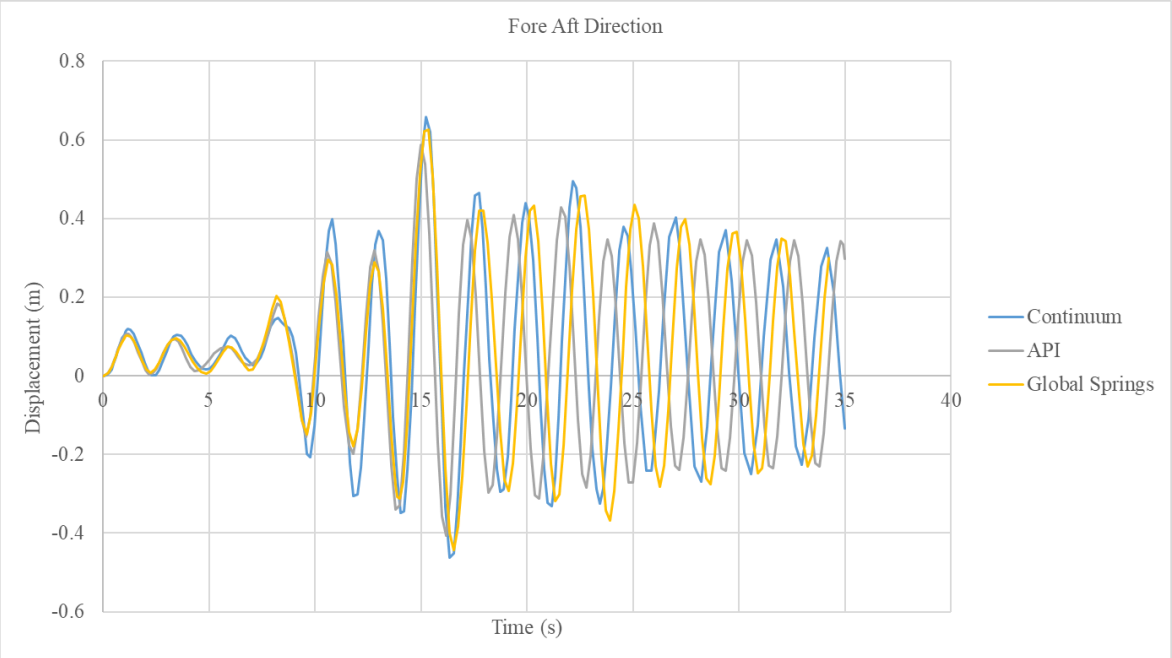

Figure 4.9. Tower Top Responses of Three Models to Kocaeli Event in Fore Aft Direction.

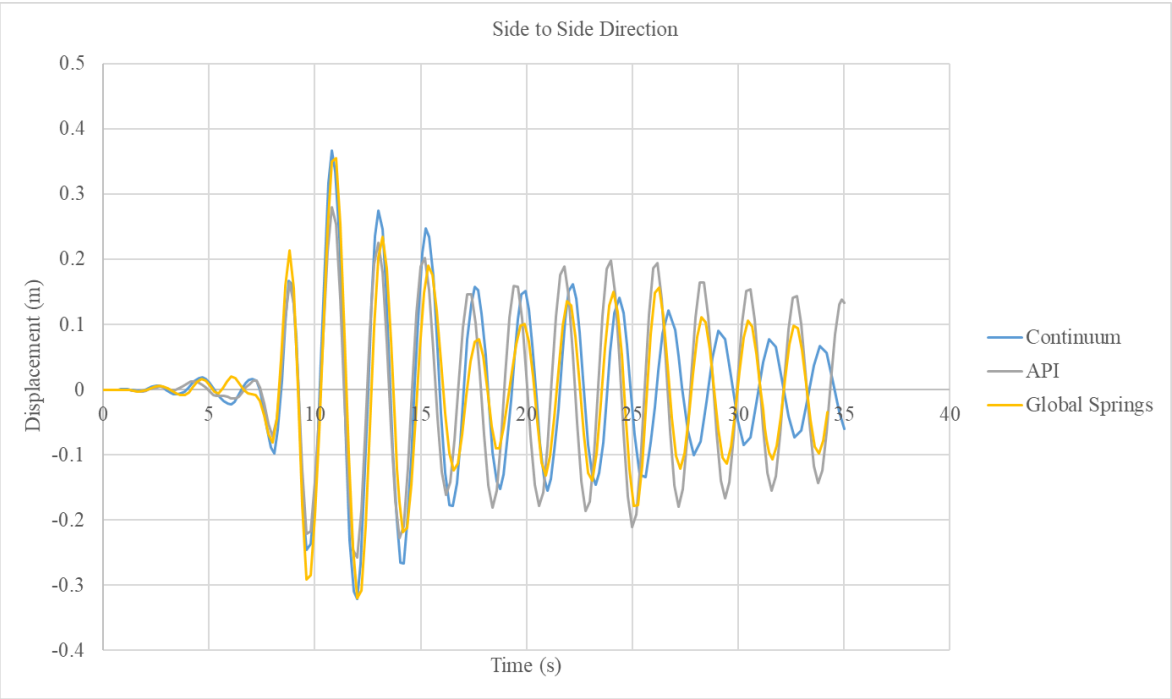

Figure 4.10. Tower Top Responses of Three Models to Kocaeli Event in Side to Side Direction.

are judged to be consistent. To further use and construct the fragility function, the model with global springs was chosen since it requires less computational time and has mode frequencies close to the identified ones. Continuum model can be considered as a reference model since it explicitly includes soil together with all other parts with detail in 3D. However, it requires to most computational time. Time is a significant matter for the analyses since each record was scaled to have SRSS PGA values as multiples of 0.05g from 0.05g to 1.00g. This requires 20 nonlinear time history analyses per record and thus 60 nonlinear time history analyses for three ground motion records.

Table 4.5. Peak Lateral Displacement Values of Three Models to Kocaeli Event.

	Peak Lateral Top Deformation (m)
Continuum Model	0.70
Global Spring Model	0.65
API Spring Model	0.62

4.3. Effect of the Ground Motion Vertical Component

The actual Turkish Seismic Design Code requires the chosen earthquake ground motion records to have 3 orthogonal components. The previous design guideline did not have this necessity. The analyses in this thesis were conducted with three component earthquake records. It was also of interest how significant the effect of the vertical component was for the response of the structure. To observe this, 3 records scaled to same SRSS PGA of 0.5g were applied to the Global Springs model with and without the vertical component. The comparison of the responses can be seen in Figures 4.11, 4.12, 4.15, 4.16, 4.13 and 4.14. For the Darfield record, the difference is noticeable in the tower displacement responses in the fore aft direction. This is due to the eccentricity of the rotor and nacelle. The inertial effects from the eccentric mass amplify the response of the structure. For the other two records however, the vertical component has almost no effect on the response. The drawn conclusion is that earthquake events with strong vertical components can be expected amplify an eccentric structure's dynamic response.

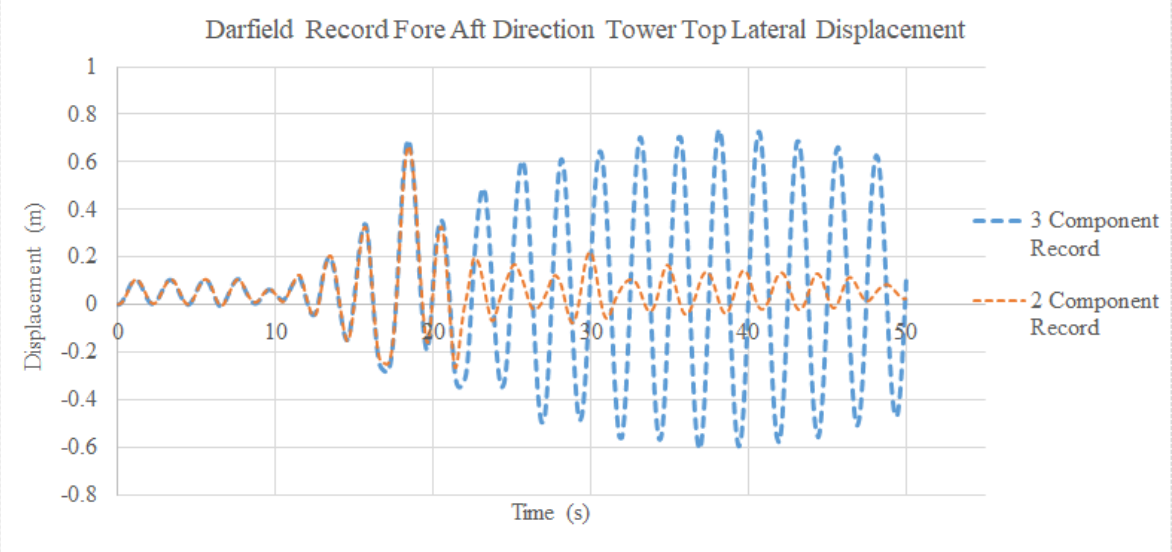

Figure 4.11. Tower Top Fore Aft Displacement Response Comparison Between 2 Component and 3 Component Darfield Record.

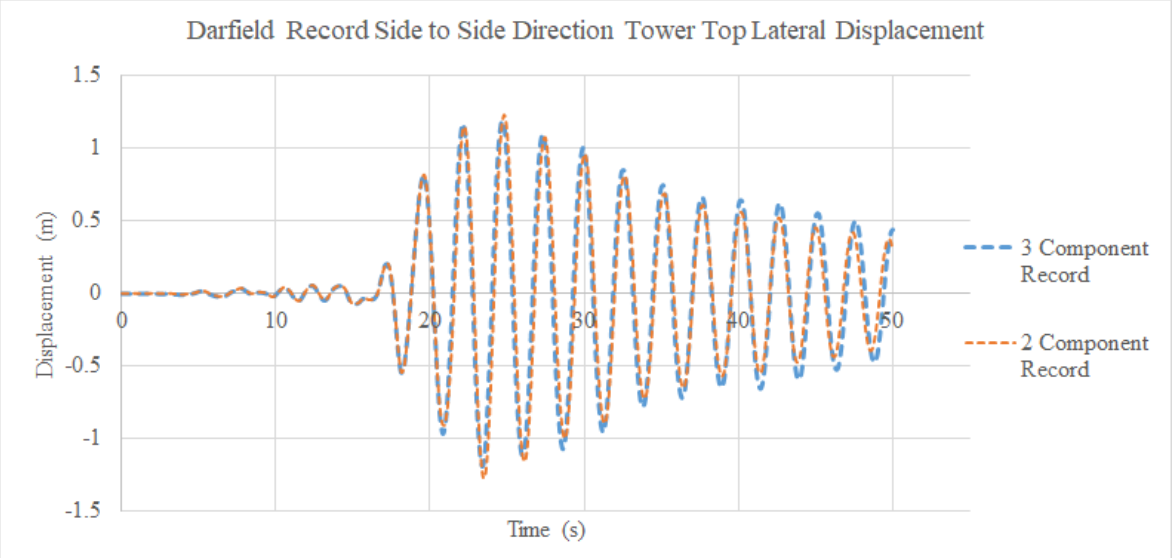

Figure 4.12. Tower Top Side to Side Displacement Response Comparison Between 2 Component and 3 Component Darfield Record.

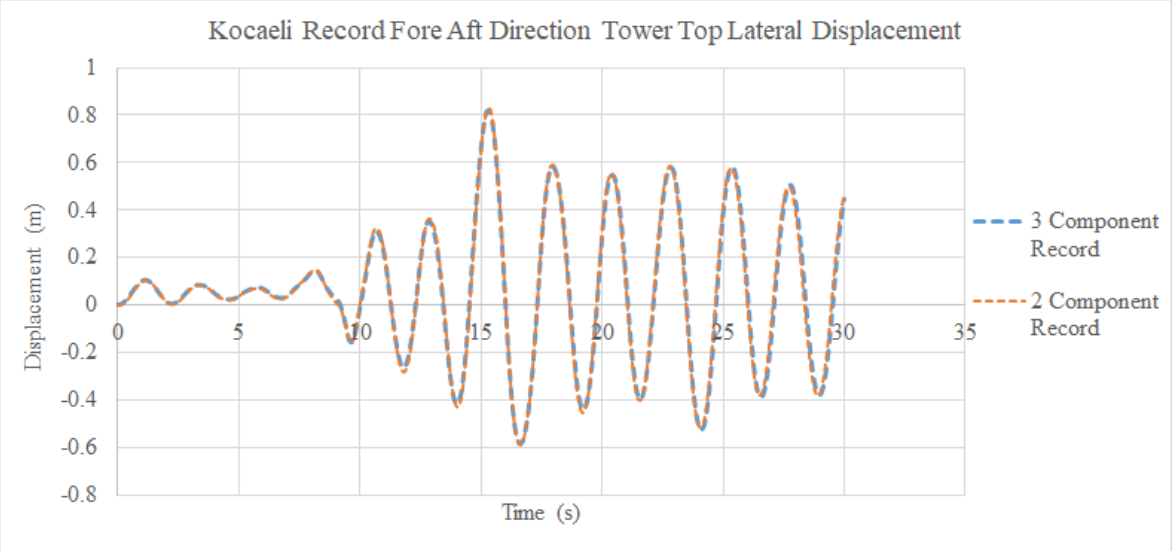

Figure 4.13. Tower Top Fore Aft Displacement Response Comparison Between 2 Component and 3 Component Kocaeli Record.

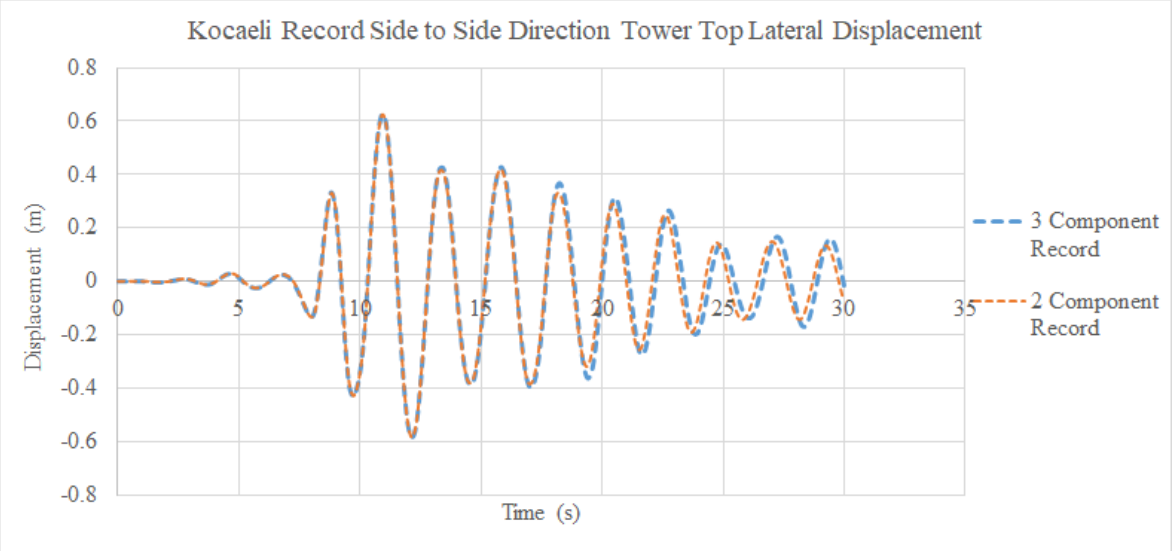

Figure 4.14. Tower Top Side to Side Displacement Response Comparison Between 2 Component and 3 Component Kocaeli Record.

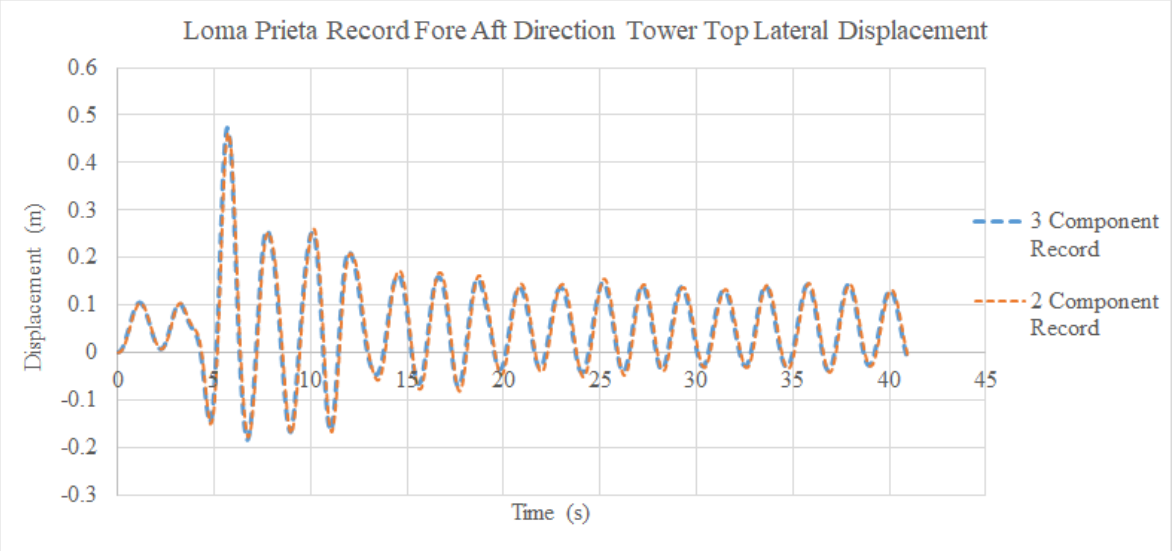

Figure 4.15. Tower Top Fore Aft Displacement Response Comparison Between 2 Component and 3 Component Loma Prieta Record.

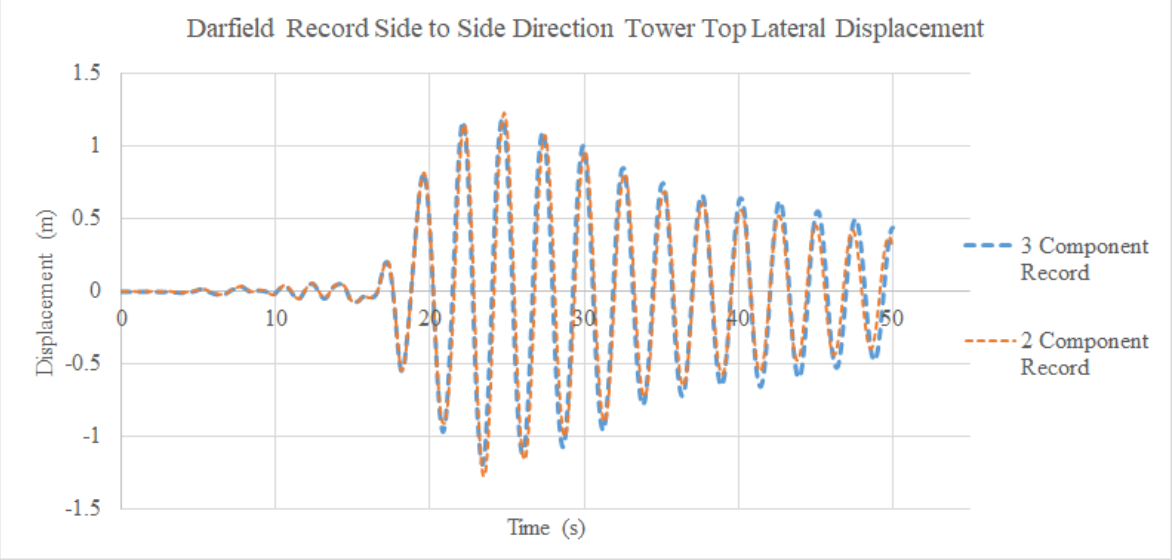

Figure 4.16. Tower Top Side to Side Displacement Response Comparison Between 2 Component and 3 Component Loma Prieta Record.

4.4. Nonlinearity in Analysis Results

Nonlinearity in the material and geometry were defined as described in previous sections. Therefore it is of interest whether the structure showed nonlinearity or stayed in linear range in responses. For this, the responses from springs in the global spring model were checked. Force deformation histories from lateral springs were obtained together with moment rotation histories from rotational springs for the global spring model subject to scaled Kocaeli record with SRSS PGA of 0.4g. The results given in Figures 4.17, 4.18, 4.19 and 4.20 showed that the lateral spring responses stayed in the linear zone whereas rotational springs outwent permanent deformations and reached the nonlinear zone.

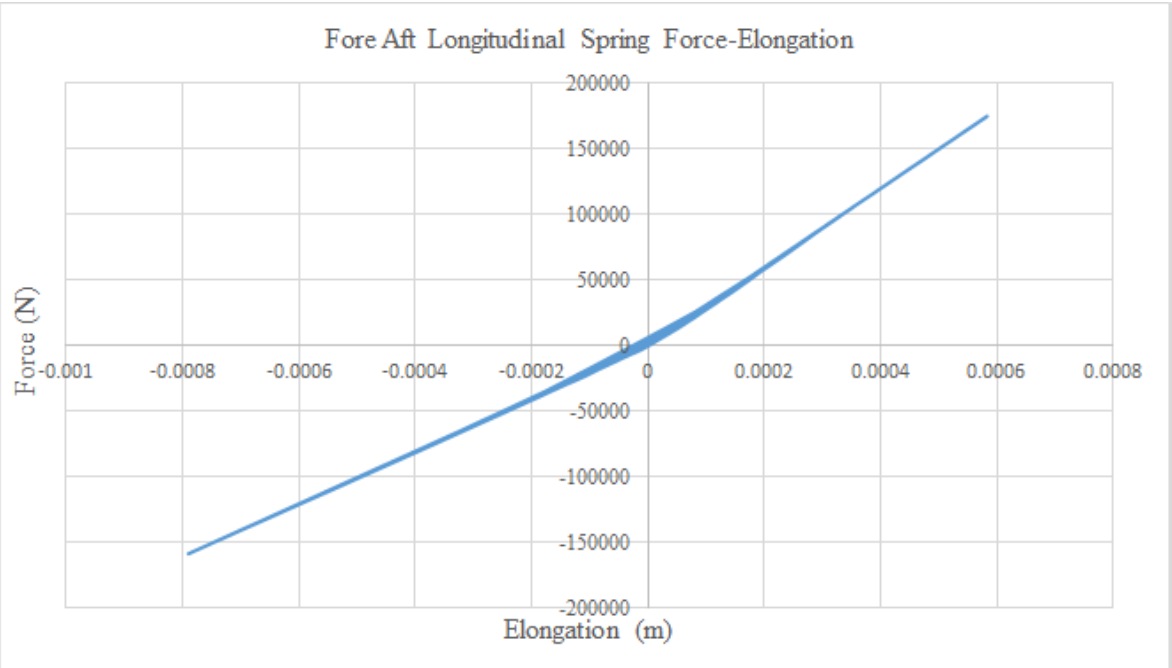

Figure 4.17. Force vs Elongation on Fore Aft Longitudinal Spring Under Kocaeli Record.

4.5. Determination of Damage States

To develop a fragility curve, one needs damage states defining the undesirable outcome of the imposed event to have a judgement of failure. Two damage states are

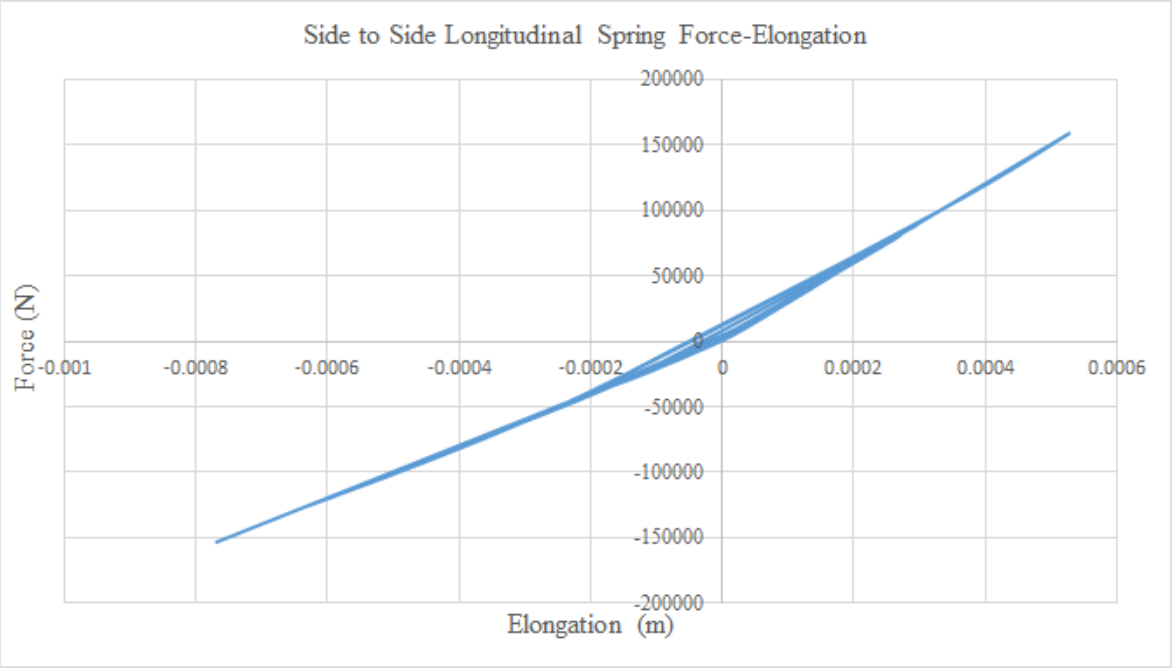

Figure 4.18. Force vs Elongation on Side to Side Longitudinal Spring Under Kocaeli Record.

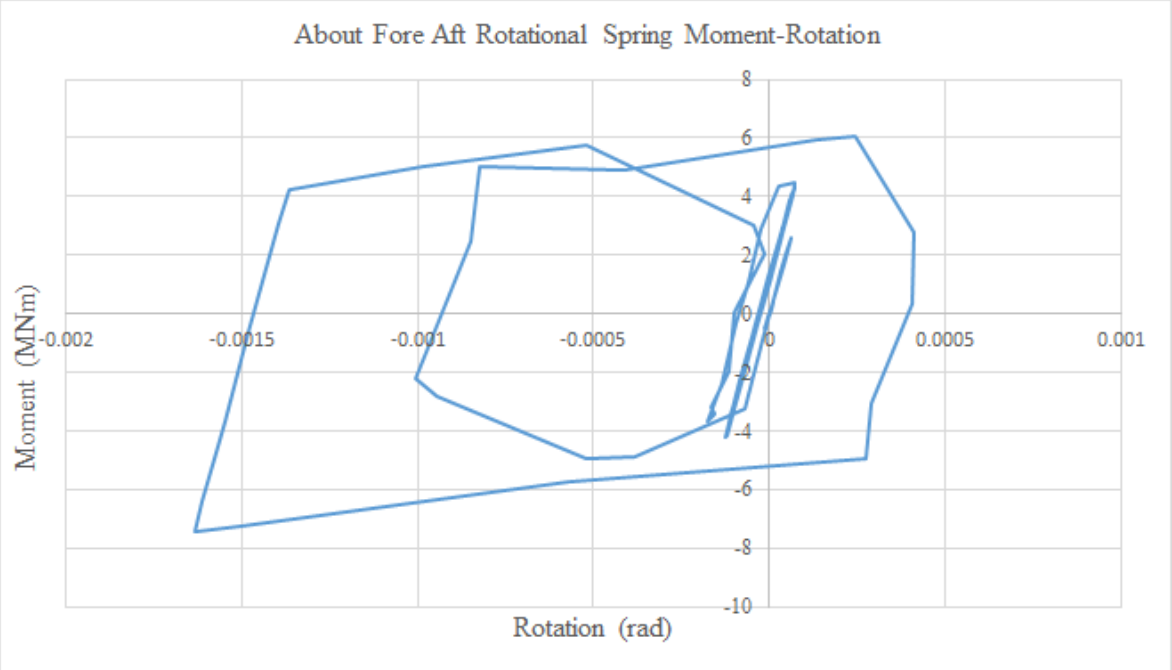

Figure 4.19. Moment vs Rotation about Fore Aft Rotational Spring Under Kocaeli Record.

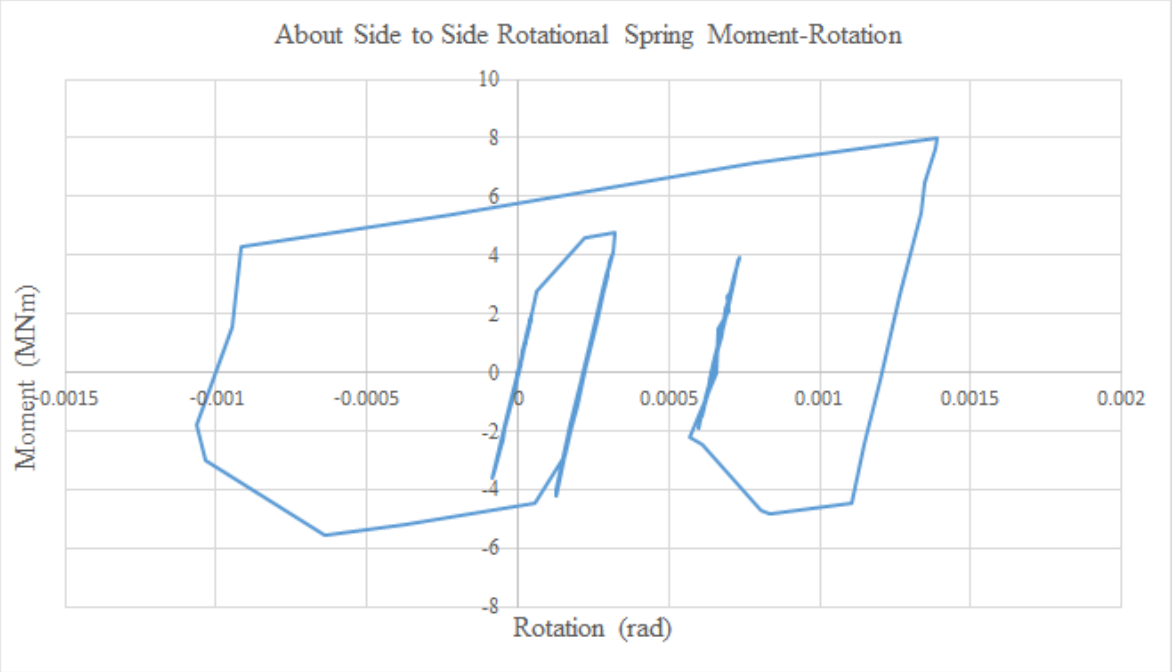

Figure 4.20. Moment vs Rotation about Side to Side Rotational Spring Under Kocaeli Record.

chosen in this thesis as local buckling of tower and a threshold hub displacement.

4.5.1. Local Buckling

The local buckling allowable stress value was calculated in accordance with the API Guideline [40]. The guideline defines two local buckling limiting stress values; elastic local buckling and inelastic local buckling. For the tubular steel sections whose outer diameter to wall thickness lies between 60 and 300, both elastic and inelastic buckling limiting stresses shall be calculated such that the smaller shall govern. For the turbine tower analyzed in this thesis, the ratio of tower width to thickness varies across the tower ranging from 83 to 138. Both values fall in the range of 60-300 therefore elastic and inelastic buckling thresholds are to be calculated and lower shall govern.

For $60 \leq D/t \leq 300$;

$$F_{xe} = \frac{2Ct}{D} \tag{4.17}$$

$$F_{xc} = F_y \left(1.64 - 0.23 \left(\frac{D}{t} \right)^{1/4} \right) \leq F_{xe} \tag{4.18}$$

where;

F_{xe}: Elastic Local Buckling Stress.

C: Critical elastic buckling coefficient with suggested value of 0.3

t: wall thickness.

D: Section Outer diameter

F_{xc}: Inelastic Local Buckling Stress

F_y: Yield Stress

For both values of D/t mentioned above, the limiting values are shown in Table 4.6. As seen from the table, lowest value is 302 MPa and thus it's chosen as local buckling threshold.

4.5.2. Hub Horizontal Displacement

The other damage state to define failure in the fragility curve is about the tower top displacement. Tower top displacement is crucial since it may lead to contact

Table 4.6. Elastic and Inelastic Local Buckling Values for Different Values of D/t.

D/t	F_{xe} (MPa)	F_{xc} (MPa)
83	1446	336
138	870	302

of tower and blades which must be avoided at all times. The limiting hub horizontal displacement was decided in accordance with the literature related to it [21, 22]. Asareh [21] in his work modelled a 5 MW wind tower with a hub height of 88 meters with elastoplastic steel elements. He also included the blades in the model explicitly. Performing pushover analysis, he suggested a limiting tower drift value of 1.25% to avoid blade tower contact. There is not a clear threshold for wind turbine tower drift under earthquake loading in guidelines. Therefore Asareh's suggestion was taken as a reference.

4.6. Fragility Curve Development

A fragility curve (FC) is a theoretical curve relating an intensity measure to the probability of exceeding a certain engineering demand parameter when subjected to that intensity measure. Fragility curves are developed by fitting a statistical cumulative distribution function to obtained data points for intensity measure vs probability of failure. The most commonly used cumulative distribution function is lognormal. It is not a must but lognormal distribution was proven to fit well to engineering statistics [50, 51]. Fragility curves are not only used in earthquake or structural engineering but many other fields as well where the reliability of a product or design is of importance. For earthquake engineering, the intensity measure can be PGA, PGD, M_w etc. For this thesis PGA is used as the intensity measure. The engineering demand parameters are chosen as local buckling of the tower and hub lateral displacement as explained in previous section.

There are three types of fragility curves and thus three ways to develop a fragility curve [18]. These are:

(i) Empirical: Empirical fragility curves are developed in accordance with the observational data from experiments or real world.

(ii) Analytical: Analytical fragility curves are formed by preparing a numerical model, subjecting it to exposures of varying intensity measures, controlling exceedance of predefined damage state and fitting a cumulative distribution for intensity measure vs. probability of failure. Analytical fragility curve is to be developed for this thesis.

(iii) Judgement Based: A judgement-based fragility curve is developed with expert opinion and knowledge about historical exposures and failures that had taken place in real world.

The form of a fragility function defined as a lognormal cumulative distribution function is as follows [52]:

$$P[C \quad | \quad IM = x] = \Phi\left(\frac{ln\left(\frac{x}{\theta}\right)}{\beta}\right) \tag{4.19}$$

where;

IM: Intensity measure (PGA).

$P[C \quad | \quad IM = x]$: The probability that a ground motion with $IM = x$ will cause the structure to collapse.

$\Phi()$: The standard normal cumulative distribution function.

θ: The median of fragility function (the PGA level with 50% probability of col-

lapse).

β: The standard deviation of $ln(IM)$.

Fitting a lognormal CDF to the data from analyses requires parameter estimation. The parameters to be estimated are θ and β. Parameter estimation is performed using maximum likelihood. The output of the time history analyses has a form such that in the horizontal axis lies the PGA values for each scaled record and in the vertical axis lies the ratio of the number of records causing damage to the number of records at that PGA value. In a way it is the probability of exceeding the damage threshold at a given intensity measure or in other words, probability of failure. Estimates of the fragility function are obtained by maximizing the likelihood value given below [52], this approach is also known as multiple stripes analysis:

$$Likelihood = \prod_{j=1}^{\mathbf{m}} \binom{n_{\mathrm{j}}}{z_{\mathrm{j}}} \Phi\left(\frac{ln\left(\frac{x_j}{\theta}\right)}{\beta}\right)^{z_{\mathrm{j}}} \left(1 - \Phi\left(\frac{ln\left(\frac{x_{\mathrm{j}}}{\theta}\right)}{\beta}\right)\right)^{n_{\mathrm{j}} - z_{\mathrm{j}}} \tag{4.20}$$

where;

x_j: Discrete IM (PGA) values.

m: Number of IM levels.

Π: Denotes a product over all levels.

n_j: Number of ground motions with $PGA = x_j$.

z_j: Number of collapses under ground motions with $PGA = x_j$.

To construct the fragility curves for this thesis, each earthquake record was scaled to have SRSS PGA values as multiples of 0.05g up until 1.00g. Then, the fractions of the limit exceeding analyses for each PGA value was plotted. Having 3 different records for each PGA value, the probabilities could be 0%, 33%, 66% or 100%. Then, to the plot of PGA vs fractional failures, a cumulative lognormal distribution function was fitted such that the likelihood as given by Equation 4.20 would maximize. The obtained failure fractions and fragility curves are given in Figures 4.21 and 4.22.

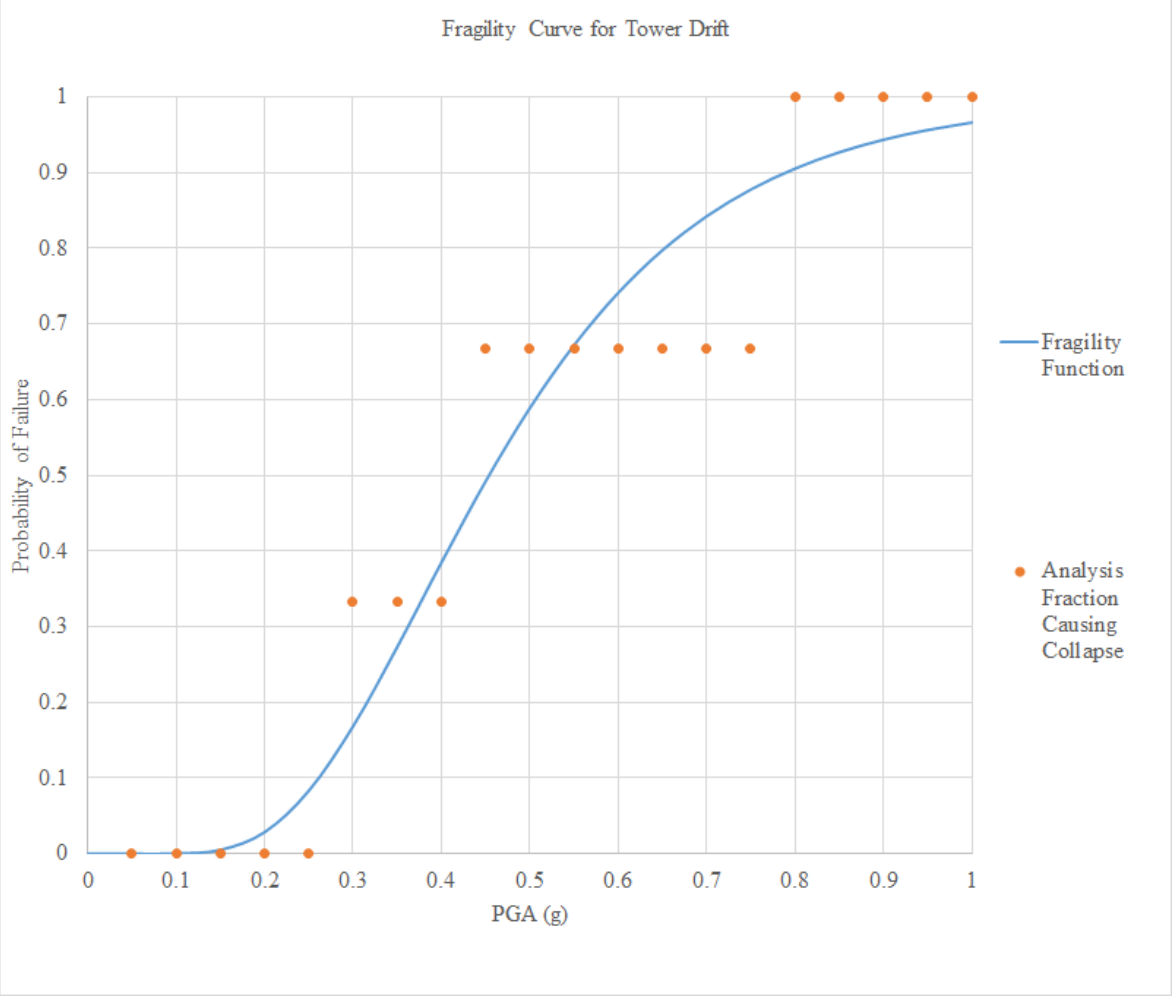

Figure 4.21. Fragility Curve for Tower Drift.

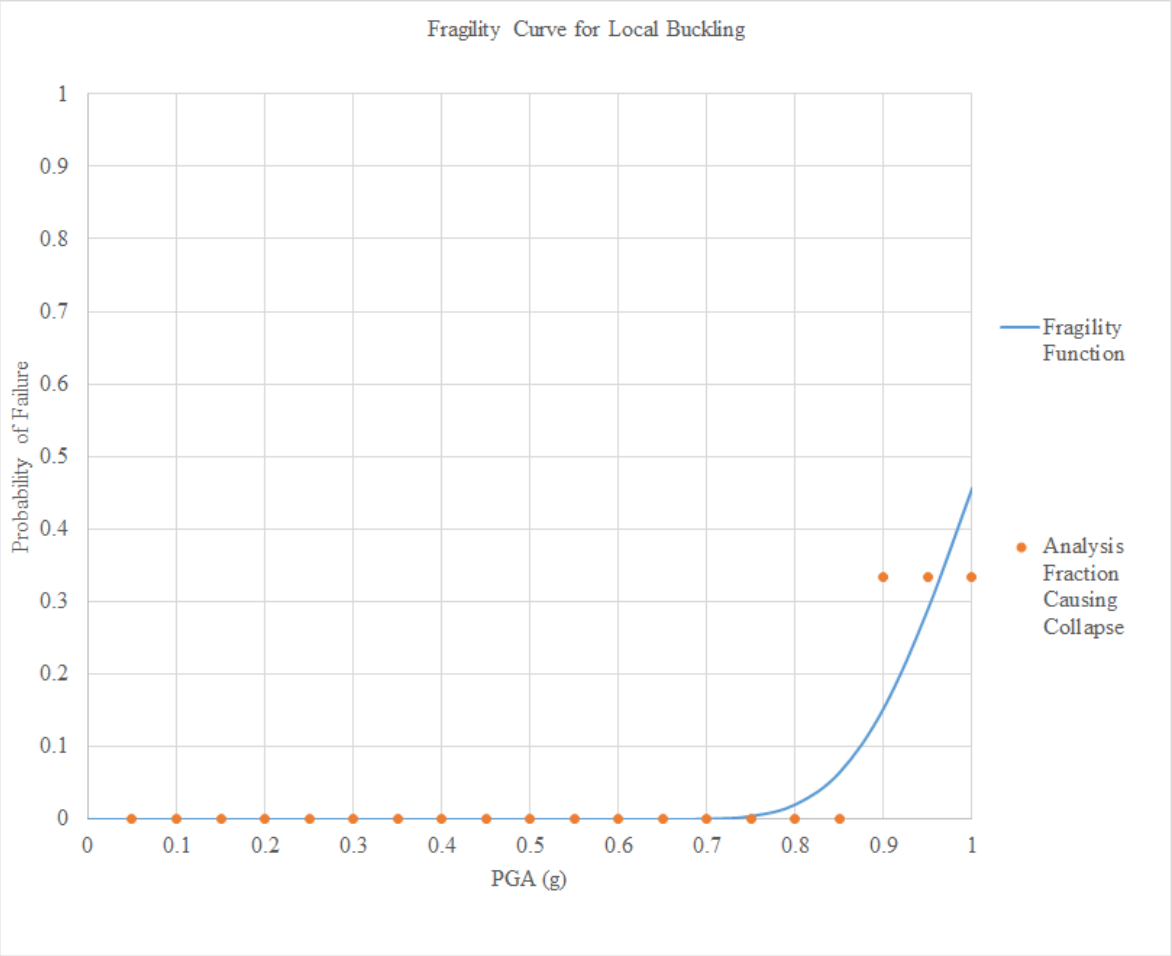

Figure 4.22. Fragility Curve for Local Buckling.

5. CONCLUSION

In this study, seismic fragility curves for an onshore wind turbine were developed considering soil-structure interaction effects. Three different modelling approaches were used and compared. The continuum model included soil, piles and tower explicitly. In this model, the nonlinearity was defined in soil material and in contacts between soil and piles. The effect of soil elasticity modulus uncertainty on the structure's modal properties was observed. Varying values of soil young's modulus were assigned and mode frequencies were compared with that obtained from FDD of the response from accelerometers on the structure. Then ground motion time history records were applied. In the global springs model, incremental static loading was applied to the continuum model's part without the tower in 3 translational and 2 rotational degrees of freedom. The obtained nonlinear load deformation relationships were attributed to the springs to be placed under the tower and then ground motion acceleration records were applied. In the API springs model, nonlinear p-y, t-z and q-z springs were defined in accordance with the API guideline and were attached to the piles with 1.5 meters distance. 1560 nonlinear springs in total were needed. Again acceleration time histories were applied to the model. Among the three models, the continuum model was taking the longest time to solve and the API springs model was the one taking most effort to create. The three models gave similar tower top maximum responses. Therefore, the global springs model was chosen to move on with the fragility analysis.

The effect of the vertical component of ground motion records on the tower top response was also examined. Three records with and without the vertical component was applied to the global springs model. Under the Darfield record, the response in side to side direction did not differ where the response in the fore aft direction amplified. This is due to the eccentricity of the point mass from nacelle and rotor. However, the responses to the other records did not modify. Therefore, the drawn conclusion herein is that some ground motion events might have amplified responses due to eccentric lump mass on the tower and three component records must be used to catch this effect.

Development of the fragility curves requires predefined limit states representing the failure of the structure. Two limit states considered in the work were local buckling as defined for tubular structures in API guidelines and tower top displacement threshold of 1.25% of tower height. The results showed the displacement limit state was governing rather than local buckling. It should be noted here that steel buckling is an ultimate limit state which would represent the total failure of the structure where the hub displacement threshold is rather an operational limit state and 1.25% tower height is taken from similar work in literature and more effort is needed to define a more concrete value for wind turbines for limiting tower drift.

The improvements to the study presented herein can be made in several means:

- Use of transmitting boundaries in the continuum model rather than fixed boundaries.
- Explicitly modelling the blades and observing their effects on modal properties.
- A detailed soil borehole log report would decrease the uncertainty related with soil mechanical properties.
- Steel tower can be modelled as nonlinear material and yielding behavior can be observed.
- More limit thresholds for tower failure can be defined.

REFERENCES

1. Erdik, M., Y. Fahjan and O. Ozel, "Istanbul Earthquake Rapid Response and the Early Warning System", *Bulletin of Earthquake Engineering*, Vol. 1, pp. 157–163, 2003.

2. Alcik, H. A., "Deprem Erken Uyarı Sistemleri", *Jeofizik Bülteni, Van Depremi ve Deprem Özel Sayısı*, Vol. 22, pp. 50–66, 2011.

3. Kausel, E. A., "Early History of Soil–Structure Interaction", *Soil Dynamics and Earthquake Engineering*, Vol. 30, pp. 822–832, 2010.

4. Díaz, O. and L. E. Suárez, "Seismic Analysis of Wind Turbines", *Earthquake Spectra*, Vol. 30, pp. 743–765, 2014.

5. Patil, A., S. Jung and O.-S. Kwon, "Structural Performance of a Parked Wind Turbine Tower Subjected to Strong Ground Motions", *Engineering Structures*, Vol. 120, pp. 92–102, 2016.

6. Lavassas, I., G. Nikolaidis and P. Zervas, "Analysis and Design of the Prototype of a Steel 1-MW Wind Turbine Tower", *Engineering Structures*, Vol. 25, pp. 1097 – 1106, 2003.

7. Bazeos, N., G. Hatzigeorgiou and I. Hondros, "Static, Seismic Stability Analyses of a Prototype Wind Turbine Steel Tower", Vol. 24, pp. 1015–1025, 2002.

8. Mensah, A., L. Dueñas-Osorio and I. Prowell, "Probabilistic Combination of Earthquake and Operational Loads for Wind Turbines", *15th World Conference on Earthquake Engineering*, 2012.

9. Nuta, E., C. Christopoulos and J. A. Packer, "Methodology for Seismic Risk Assessment for Tubular Steel Wind Turbine Towers: Application to Canadian Seismic

Environment", *Canadian Journal of Civil Engineering*, Vol. 38, pp. 293–304, 2011.

10. Witcher, D., "Seismic Analysis of Wind Turbines in the Time Domain", *Wind Energy*, Vol. 8, pp. 81–91, 2005.

11. Zaaijer, M., "Foundation Modelling to Assess Dynamic Behaviour of Offshore Wind Turbines", *Applied Ocean Research*, Vol. 28, pp. 45 – 57, 2006.

12. Katsanos, E. I., S. Thöns and C. Georgakis, "Wind Turbines and Seismic Hazard: A State of the Art Review", *Wind Energy*, Vol. 19, pp. 2113–2133, 2016.

13. Prowell, I., M. Veletzos and A. Elgamal, "Experimental and Numerical Seismic Response of a 65 kW Wind Turbine", *Journal of Earthquake Engineering*, Vol. 13, pp. 1172–1190, 2009.

14. Taddei, F., M. Schauer and L. Meinerzhagen, "A Practical Soil-Structure Interaction Model for a Wind Turbine Subjected to Seismic Loads and Emergency Shutdown", *Procedia Engineering*, Vol. 199, pp. 2433 – 2438, 2017.

15. Austin, S. and S. Jerath, "Effect of Soil-Foundation-Structure Interaction on the Seismic Response of Wind Turbines", *Ain Shams Engineering Journal*, Vol. 8, pp. 323 – 331, 2017.

16. Prowell, I., A. Elgamal and J. Lu, "Modelling the Influence of Soil-Structure Interaction on the Seismic Response of a 5-MW Wind Turbine", *Fifth International Conference on Recent Advances in Geotechnical Earthquake Engineering and Soil Dynamics.*, 2010.

17. Kennedy, R., C. Cornell and R. Campbell, "Probabilistic Seismic Safety Study of an Existing Nuclear Power Plant", *Nuclear Engineering and Design*, Vol. 59, pp. 315 – 338, 1980.

18. Porter, K., *A Beginner's Guide to Fragility, Vulnera-*

bility, and Risk, University of Colorado Boulder, 2018, http://spot.colorado.edu/ porterka/Porter-beginners-guide.pdf, accessed at June 2018.

19. Mylonakis, G. and G. Gazetas, "Seismic Soil-Structure Interaction: Beneficial or Detrimental?", Vol. 4, pp. 277–301, 2000.

20. Wang, S., B. L. Kutter and M. J. Chacko, "Nonlinear Seismic Soil Pile Structure Interaction", *Earthquake Spectra*, Vol. 14, pp. 377–396, 1998.

21. Asareh, M. A., *Dynamic behavior of operational wind turbines considering aerodynamic and seismic load interaction*, Ph.D. Thesis, Missouri University of Science and Technology, 2015.

22. Mo, R., H. Kang and M. Li, "Seismic Fragility Analysis of Monopile Offshore Wind Turbines under Different Operational Conditions", *Energies*, Vol. 10, 2017.

23. Recreational Aircraft Association of New Zealand, *Lift*, http://raanz.org.nz/wiki/pmwiki.php?n=TM.Principals, accessed at June 2018.

24. Dodge, D. M., "Illustrated history of wind power development", http://telosnet.com/wind/, accessed at June 2018.

25. Allamehzadeh, H., "Wind Energy History, Technology and Control", pp. 119–126, 2016 IEEE Conference on Technologies for Sustainability (SusTech), 2016.

26. The Stuttgart Buch, *Wind as Energy Source*, http://www.stuttgart-buch.de/change-in-mobility/wind-as-energy-source.html, accessed at June 2018.

27. Renewable Energy Network for 21st Century, *Renewables 2018, Global Status Report*, 2018.

28. GWEC, *Wind Power Leading the Charge to Drive Out Fossils*, 2017, http://gwec.net/wind-power-leading-the-charge-to-drive-out-fossils/, accessed at June 2018.

29. Wind Europe, *Wind in Power 2017, Annual Combined Onshore and Offshore Wind Energy Statistics*, 2017.

30. GWEC, *Annual Market Update, Global Wind Report*, 2017.

31. TBMM, *Yenilenebilir Enerji Kaynaklarının Elektrik Enerjisi Üretimi Amaçlı Kullanımına İlişkin Kanun*, http://www.mevzuat.gov.tr/MevzuatMetin/1.5.5346.pdf, accessed at June 2018.

32. *Turkish Wind Energy Statistics Report*, Tech. rep., TWEA, 2018.

33. Kadirioğlu, F. T., R. F. Kartal and T. Kılıç, "An Improved Earthquake Catalogue ($M \geq 4.0$) for Turkey and Its Near Vicinity (1900–2012)", *Bulletin of Earthquake Engineering*, Vol. 16, pp. 3317–3338, 2018.

34. Barka, A., H. S. Akyuz and E. Altunel, "The Surface Rupture and Slip Distribution of the 17 August 1999 I˙zmit Earthquake (M 7.4), North Anatolian Fault", *Bulletin of the Seismological Society of America*, Vol. 92, pp. 43–60, 2002.

35. Duman, T. Y., O. Emre and A. Dogan, "Step-Over and Bend Structures along the 1999 Duzce Earthquake Surface Rupture, North Anatolian Fault, Turkey", *Bulletin of the Seismological Society of America*, Vol. 95, pp. 1250–1262, 2005.

36. Emre, Ö., T. Y. Duman and S. Özalp, "Active fault database of Turkey", *Bulletin of Earthquake Engineering*, Vol. 16, pp. 3229–3275, 2018.

37. AFAD, *Earthquake Hazard Map of Turkey*, 2018.

38. YEGM, *Turkey Wind Energy Potential Map*,

http://www.yegm.gov.tr/YEKrepa/REPA-duyuru01.html, accessed at June 2018.

39. TUREB, *Installed Wind Power Plants in Turkish Cities*, http://cografyaharita.com/turkiyeenerjiharitalari.html, accessed at June 2018.

40. American Petroleum Institute, *Recommended Practice for Planning, Designing and Constructing Fixed Offshore Platforms—Working Stress Design*, 2002.

41. Uesugi, M., H. Kishida and Y. Uchikawa, "Friction Between Dry Sand and Concrete Under Monotonic and Repeated Loading", *Soils and Foundations*, Vol. 30, pp. 115–128, 1990.

42. Brincker, R., L. Zhang and P. Andersen, "Modal Identification of Output Only Systems Using Frequency Domain Decomposition", *Smart Materials and Structures*, Vol. 10, pp. 441–445, 2001.

43. Das, B. M., *Principles of Geotechnical Engineering, 7th Edition*, Cengage Learning, 2010.

44. ANSYS, Inc., *ANSYS Reference Article*.

45. O'Neill, M. W. and J. M. Murchinson, *An Evaluation of p-y Relationships in Sands*, Tech. rep., University of Houston, Texas, 1983, report to the American Petroleum Institute.

46. Matlock, H., "Correlations for Design of Laterally Loaded Piles in Soft Clay.", *Proceedings of the 2nd Offshore Technology Conference, Houston,*, pp. 577–594, 1970.

47. Reese, L., W. Cox and F. Koop, "Field Testing and Analysis of Laterally Loaded Piles on Stiff Clay", *Proceedings of the 7th Offshore Technology Conference*, Vol. 2,

1975.

48. Kraft, L. M., W. R. Cox and E. A. Verner, "Pile Load Tests: Cyclic Loads and Carrying Load Rates.", *Journal of Geotechnical Engineering, ASCE*, Vol. 107, pp. 1–19, 1981.

49. AFAD, *Turkish Earthquake Resistant Building Code*, 2018.

50. Ibarra, L. F. and H. Krawinkler, *Global Collapse of Frame Structures Under Seismic Excitations.*, Tech. rep., The John A. Blume Earthquake Engineering Center, Stanford University, 2005.

51. Porter, K., R. Kennedy and R. Bachman, "Creating Fragility Functions for Performance-Based Earthquake Engineering", *Earthquake Spectra*, Vol. 23, pp. 471–489, 2007.

52. Baker, J. W., "Efficient Analytical Fragility Function Fitting Using Dynamic Structural Analysis", *Earthquake Spectra*, Vol. 31, pp. 579–599, 2015.